Chapter 4. *In situ* transmission experiments

In *Chapter 3 in situ* techniques were identified as the most reliable technique for measuring the geoacoustic properties of a well-defined volume of sediment, with the ideal features of a transmission experiment discussed in *Section 3.2.* In order to perform such a suite of experiments in a range of sediment types a new acoustic device, the Sediment Probing Acoustic Detection Equipment (SPADE) has been developed. This consists of two types of *in situ* acoustic probes: a piezoceramic source and a set of matched receivers, both of which can be inserted into seafloor sediments. This device can emit and detect compressional wave pulses with central frequencies within the operational frequency range of 16 to 100 kHz. The SPADE was used to perform a suite of *in situ* transmissions tests on inter-tidal sediments, with the sites examined incorporating a wide range of sediment types. The examination of two to four closely spaced locations at each site allows the effects of the sediment variability (discussed in *Sections 2.4.1* and *2.4.2*) on measured geoacoustic properties to be examined.

4.1. The SPADE

The SPADE was developed by the Challenger and Ocean Engineering Divisions at Southampton Oceanography Centre. The production of the source element was undertaken by Piezo Ceramic Transducers Ltd., based in Aberdeen, in 1999, who also produced a set of matched receivers between January and May, 2002. The electronic components of the SPADE were designed and built by the Ocean Engineering Division at Southampton Oceanography Centre.

The source, *Figure 4.1,* consists of a curved section of piezoceramic element. As this possesses a resonant frequency greater than 200 kHz (Harris, 2001) the source operates in an untuned manner over the usable frequency range of 16 to 100 kHz. The considerable degree to which a broadband pulse can be distorted by a tuned transducer has been discussed in *Section 3.2.4.* For the pulses utilised within this project, see *Section 4.2,* the untuned mode of operation should minimise these distortions, a feature which is essential to the processing techniques applied, *Section 5*. The frequency range of 16 to 100 kHz extends that over which the majority of previous *in situ* transmission experiments span, *i.e.* less than 50 kHz. The transducer element is embedded in a plastic mould, with a

height of 158 mm, width of 109 mm, and thickness of 10 mm, which is supported by an aluminium surround. The purpose of the mould and surround are to protect and support the element during the deployment of the device. The original rationale behind the curved nature of the device was to mimic a garden spade and so aid insertion into the sediment. The pressure fields emitted are examined in detail in *Section 4.3.* The source is attached to a 2 m long aluminium channel to aid deployment, *Figure 4.2*. The aluminium channel consists of a front section, 76 mm wide, and two strengthening side sections, both 38 mm deep. With the present manual deployment method used, this limits the maximum depth of insertion to approximately 1 m.

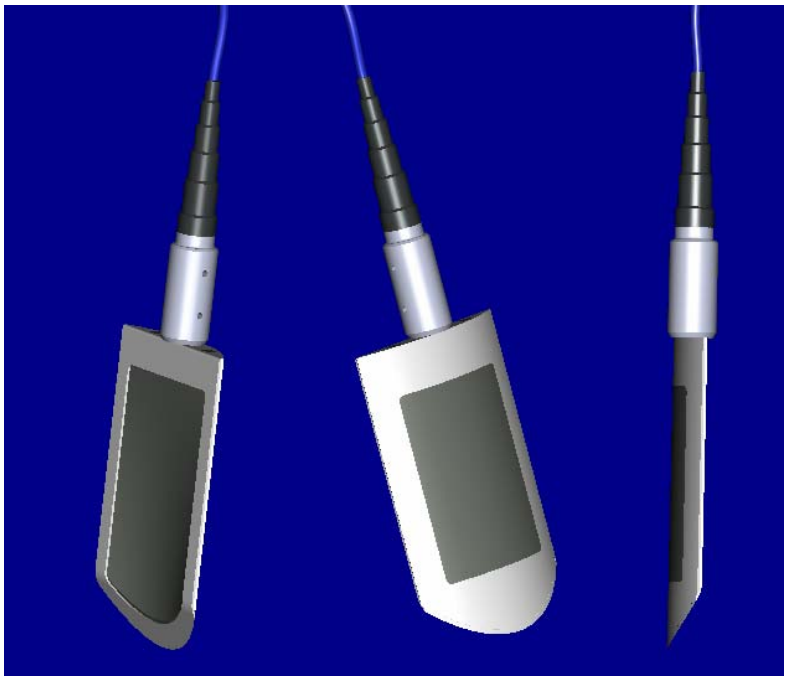

Figure 4.1. Image of the source element, viewed from three angles. Both the black plastic mould, whose physical dimensions are a height of 200 mm and a width of 120 mm, and the aluminium surround are visible, while the convex emitting face is clearly displayed in the central image.

Neither the emitted pressure field or the transmit voltage response (TVR), which is the level of acoustic output at a distance of 1 m from the source relative to 1 V input, were available from the manufacturer. The emitted pressure field, which enables the calculation of spreading losses and is necessary to calculate attenuation coefficient, was therefore

modelled (*Section 4.3),* while the processing applied does not require knowledge of the TVR.

Initial field trials of the SPADE used an air backed hemispherical barium titanate receiver, which was embedded in silicone elastomer to enhance coupling to the sediment. However, this receiver possessed a resonant frequency of 80 kHz, which caused distortions in the received signal. Consequently a set of matched receivers were produced, *Figure 4.3,* whose physical dimensions were a height of 119 mm, width of 58 mm and thickness of 23 mm. These were covered in a polyurethane coat with a thickness of 2 to 3 mm, in order to protect the elements and enhance coupling to the sediment.

The receivers were attached to similar aluminium channels as those used for the source. These were placed in pre-cut holes in the front section of the channels, *Figure 4.2,* and secured in place using polyurethane marine sealant. This manner of attachment minimised any acoustic reflections from the supporting channel, while providing a secure position for the receiver elements.

Figure 4.2. Source (left) and Receiver (right) attached to aluminium channels. The measuring pole in centre denotes scale, with each taped section measuring 10 cm long.

Figure 4.3. Receiver element embedded in polyurethane mould.

More information was available about the receivers than for the source. The receiver sensitivity, *Figure 4.4,* was measured from 1 to 100 kHz by Drumgrange Ltd., based in Portland, Dorset. The errors are stated to be $\pm$ 1 dB for frequencies greater than or equal to 3 kHz, while the errors for frequencies less than 3 kHz are simply stated as larger than $\pm$ 1 dB, due to the physical size of the projector used. Over the frequency range of 16 to 100 kHz, the receiver sensitivity varies by less than 9 dB and displays no resonant frequencies. This approximates to the ideal flat response required to prevent the receivers used from distorting the waveforms detected.

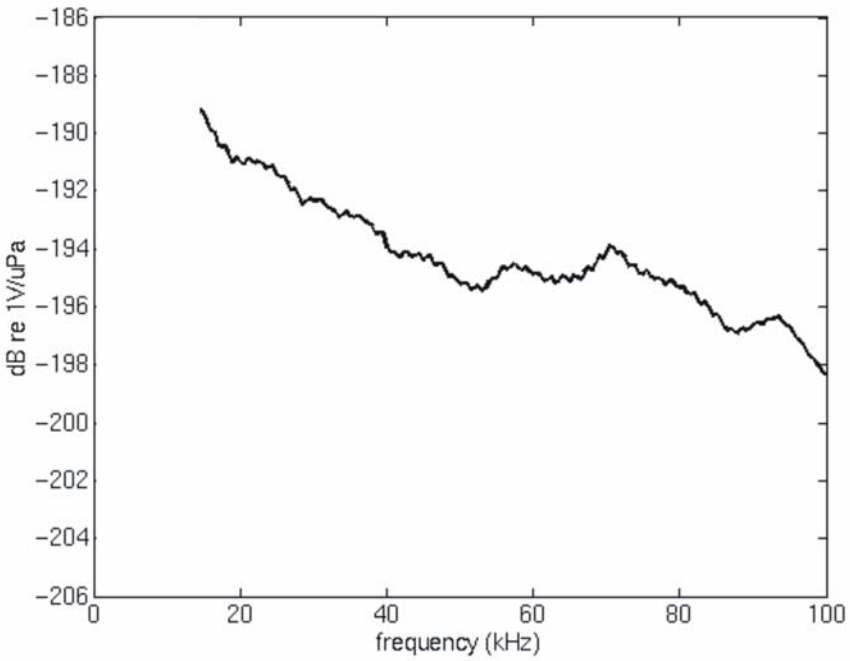

Figure 4.4. Receiver sensitivity from 16 to 100 kHz, measure in dB re. 1 V/µPa @ 1 m.

Predicted beam responses were also calculated by the manufacturer. These were calculated for the horizontal plane which intercepts the centre of the receiver at a distance of 100 mm from the receiver. One degree increments from – 90^{o} to + 90^{o} were examined at frequencies of 1 and 100 kHz only (*Figure 4.5)*. At both frequencies, the response is a maximum at 0^{o}. At 1 kHz the beam response is almost omni-directional, with a maximum difference of 0.07 dB over the full range of angles. However, at 100 kHz, the beam response depends strongly on angle, displaying thirteen peaks and twelve nulls from – 90^{o} to + 90^{o}. Though the frequency of 1 kHz is outside the operational range of the SPADE, *Figure 4.5* displays the enhanced dependence of the receiver beam response on angle as frequency increases. Small deviations in the angle of the receiver face will therefore have an increased effect on the amplitude of the received signal as frequency increases. A detailed examination of the errors expected from both variations in the orientation of the receiver face and the coupling of the receiver to the sediment is undertaken in *Section 5.3.2.*

Ideally receiver sensitivities should be determined in the far field. The near-to-far field transitions of the receiver can be estimated using *Equation 4.12* and a velocity of 1470 m·s^{-1} (see *Section 4.3.2*) and vary from 2.4 mm at 1 kHz to 236 mm at 100 kHz. Therefore, while the receiver sensitivity determined at 1 kHz is valid for the far-field, the

receiver sensitivity for 100 kHz is more applicable to the near-field, with its relevance to the far-field unable to be determined. As the height of the receiver is twice the width, the vertical directivity of the receiver will also be more pronounced than the horizontal directivity displayed in *Figure 4.5*. This factor of two indicates that the dependence of the beam response on angle in the vertical will be twice as pronounced as that displayed for the horizontal.

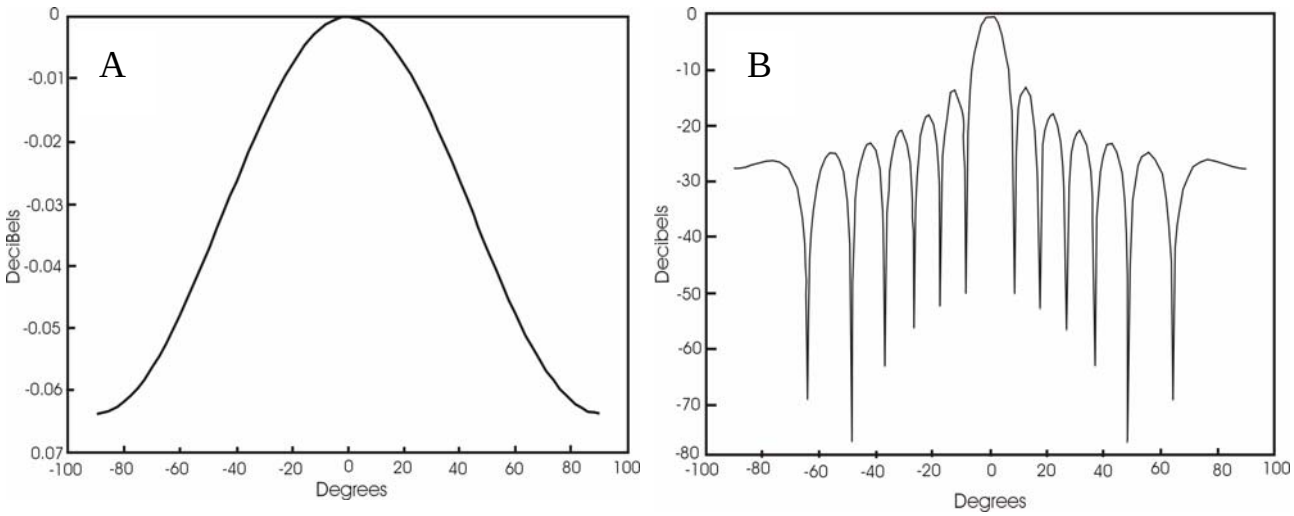

Figure 4.5. Predicted beam responses of the receivers at 1 kHz (A) and 100 kHz (B) measured in dB relative to 0^o.

The relatively large surface areas of the active faces of the source and receiving transducers, *i.e.* 172 cm^2 and 69 cm^2, are much greater than those possessed by previous *in situ* devices, which quote dimensions less than 12.3 cm^2. The increased contact area will enhance the repeatability the coupling of the SPADE to the sediment, and hence enable variations in the amplitude of the received signals to be more reliably related to sediment attenuation.

In order to allow the pulse transmitted though the sediment to be detectable, the electronic signals required amplification before emission from the source transducer and after detection by the receiver. The details of the corresponding source and receiver amplifiers are discussed below.

The electronic pulse incident from the source transducer, *i.e.* the *voltage output pulse,* was generated by transmitting a pre-programmed pulse, *i.e.* the *voltage input pulse*, through the source amplifier. This amplifier possessed an operational bandwidth of 16 to

100 kHz, with electronic pulses having central frequencies less than 16 kHz being distorted by the source amplifier, while those with central frequencies greater than 100 kHz not undergoing sufficient amplification for effective propagation through the required S-R separations used in the fieldwork. The limitations of the source amplifier was the primary factor controlling the operational bandwidth of the SPADE. The source amplifier required both a high and a low voltage supply, which were regulated to $\pm$ 62 V and $\pm$ 12 V respectively in order to prevent varying battery power from affecting the *voltage input pulse.* These supplies were provided by seven, 12 V lead acid batteries housed in a separate aluminium box.

The acoustic signals detected by the receivers were passed through the receiver amplifier in order to increase its amplitude. These amplifiers were adjusted to a gain of approximately 60 dB, varying by less than 1.4 dB over the usable frequency range of 16 to 100 kHz, *Figure 4.6.* The receiver amplifier was powered by a 10 V d.c. supply, which was provided by two 12 V lead acid batteries housed in a separate aluminium box. This amplifier was attached to the top of the aluminium channel used to deployed the receiver (*i.e.* the grey box labelled "1" in *Figure 4.32B)* and was susceptible to knocks during deployment. In order to measure the possible effects of such alterations, the gain of the receiver amplifiers were checked on a weekly basis, with the maximum discrepancy between consecutive checks being less than 0.3 dB.

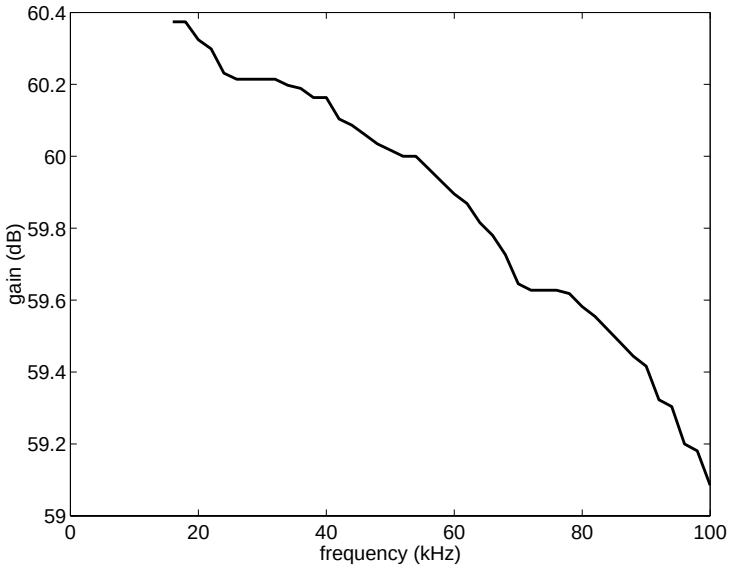

Figure 4.6. Typical electronic gain of receiver amplifiers over operational frequency range of 16 to 100 kHz.

The acquisition device consisted of a standard IBM compatible pc, which was powered using a 1 kW inverter running off two 12 V car batteries connected in series. A LabVIEW^{TM} based acquisition programme was used to acquire the data. A sampling frequency of 1 MHz was used, which allowed ten data points per oscillation at the highest central frequency used. The acquisition programme was triggered using the falling edge of a pre-programmed square wave. For all central frequencies, the centre of the *voltage input pulse* was synchronised to occur 700 μs after this falling edge. As the source amplifier incurred phase delays of less than 1 μs, the centre of the *voltage output pulse* impinges on the source transducer exactly 700 μs after the acquisition commences, *Figure 4.7.* This acquisition procedure provides a reliable reference time from which arrival times and velocities can be calculated. In addition to the signals detected by the two receivers, both the *voltage output pulse* and the square trigger wave were recorded, with a duration of 8 ms recorded in each case.

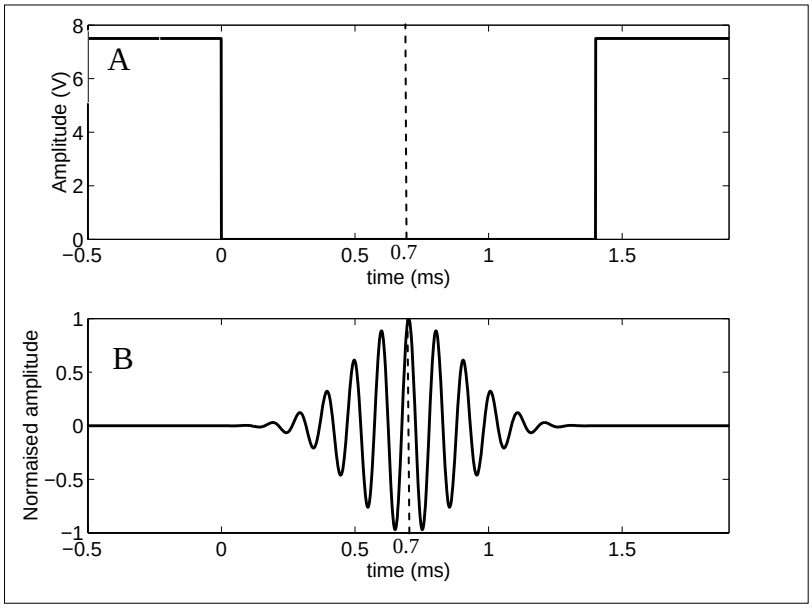

Figure 4.7. Pre-programmed waves including square wave used to trigger acquisition (A) and voltage output pulse sent to source transducer (B). Both are plotted relative to zero time, which is defined by the falling edge of the square wave, with centre of square and voltage input wave denoted by dashed lines.

4.2. Tonal pulses used

Tonal pulses, with central frequencies ranging from 16 to 100 kHz in steps of 2 kHz were selected to examine the sediment. Careful consideration was given to the durations and envelopes of these pulses and the parameters which were allowed to vary with frequency.

As discussed in *Section 4.1*, the procedure used to generate the emitted acoustic pulse involves inputting a pre-programmed *voltage input pulse* into the source amplifier. The *voltage output pulse* emitted from the source amplifier will possess a different shape and amplitude to the *voltage input pulse*. The *voltage output pulse* is then sent to the source transducer, where it is converted into an acoustic pulse. Again the envelope of the acoustic pulse emitted from the source transducer will be modified from that of the *voltage output pulse*.

Ideally, at each central frequency used, the acoustic pulse emitted from the source will contain the same number of oscillations and possess the same amplitude envelope. This will ensure that any frequency-dependent variations in the amplitude or shape of the detected pulse can be related to the dispersion and attenuation of the sediment through which the acoustic wave has propagated.

One manner of generating acoustic pulses with known amplitudes and envelopes involves the pre-distortion of the voltage signals sent to the source transducer, in such a way that the distortions of the source transducer are counteracted (Quinn, 1997). This approach requires knowledge of both the voltage signal applied to the source transducer and the acoustic pulse emitted by it, the latter of which is generally measured in calibration tests performed in water. For the higher central frequencies of 72 to 100 kHz used in this project, the power settings required to allow effective signal detection in sediment resulted in the acoustic pulses emitted into water being too large to be measured, *i.e.* clipping occurred at the receiver. Hence the emitted acoustic wave could not be measured at the correct power settings and the calculation of pre-distortions was not possible, within the time frame of this project.

The approach adopted was to generate pre-programmed *voltage input pulses* which possessed a common number of cycles and a common envelope for each central frequency examined. As discussed earlier in this section, the envelope and amplitude of the acoustic pulses emitted will vary with central frequency, due to the distortions of the source

amplifier and the source transducer. The processing techniques developed in *Sections 5.2.1* and *5.3.1* utilise both the *voltage output pulse* and the acoustic pulse emitted by the source. Hence the following sections present the properties of the *voltage input pulse,* the *voltage output pulse* and acoustic pulses transmitted through water, with the acoustic pulses transmitted through sediment discussed in *Section 5.2.2.*

4.2.1. Properties of *voltage input pulse*

It was advantageous to use a *voltage input pulse* with a smooth envelope function, as this reduced the presence of superfluous frequencies which are generated by sharp transitions and discontinuities. Such distortions have been noted in literature to produce emitted acoustic waves which differ considerably from the voltage pulses applied to the source transducer (Buckingham and Richardson, 2002). A range of modulation envelopes was examined, in order to locate an envelope which possessed the following ideal characteristics:

- A smooth time-envelope.
- A sharp spectral envelope, *i.e.* a narrow bandwidth, which allows the acoustic properties measured to be more reliably attributed to the central frequency of the pulse.
- A sharp autocorrelation, which will reduce the errors in the observed arrival times obtained by the processing techniques used, *Section 5.2.1.*

The optimum spectral envelope identified was the Blackman-Harris envelope. This is the envelope used in chirp profiling (Schock *et al.*, 1989), with the spectral amplitude *W(f)* at a frequency *f* given by

$$W(f) = 0.35875 - 0.48829\cos\left(\frac{2\pi}{N_1} f\right) + 0.14128\cos\left(\frac{2\pi}{N_1} 2f\right) - 0.01168\cos\left(\frac{2\pi}{N_1} 3f\right) \qquad 4.1,$$

where $f = 0, 1, 2\ldots N_1\text{-}1$ and N_1 is the number of samples in the Blackman-Harris window, which increases from 36 to 221 as the central frequency increases from 16 to 100 kHz.

The required *voltage input pulses* were generated by creating symmetrical spectra, *i.e.* amplitude spectra in the negative frequency domain are the mirror image of those in the positive frequency domain. This was transformed to the time-domain using an Inverse Fast Fourier transform and time shifted to form the correct pulse.

The product of the duration of the *voltage input pulse* T_i and the central frequency of the voltage input pulse f_i was kept constant for all central frequencies. The duration is defined by the time between the two half-amplitude points, *Figure 4.8.* This is equivalent to keeping the number of oscillation per pulse constant, irrespective of the central frequency. This is expressed as

$$T_i f_i = {}^{T_i}\!/_{\tau_i} \qquad 4.2,$$

where τ_i is the period.

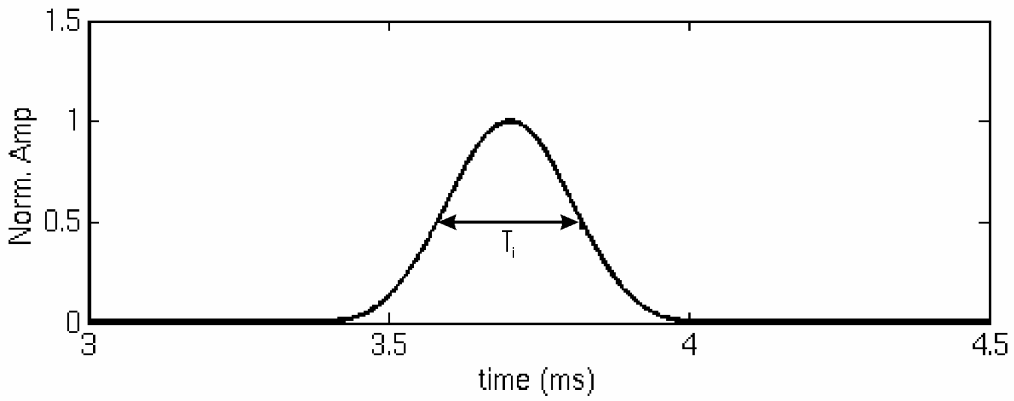

Figure 4.8. Definition of duration T_i of voltage input pulse, which is defined as time between two half-amplitude points.

A typical *voltage input pulse* is displayed in *Figure 4.9A*, with all pulses containing approximately ten oscillations. As required, this has a smooth envelope (*Figure 4.9A)* and an amplitude spectrum which possesses a narrow bandwidth and negligible sidelobes (*Figure 4.9B).* The autocorrelation (*Figure 4.9C)* is broader than desired, with a duration greater than that of the pulse itself. Though this is less than ideal, it is an intrinsic property of tonal pulses which possess smooth envelopes. The use of alternative envelope functions, *e.g.* cosine and cosine squared functions, did not significantly reduce the breadth of the autocorrelation.

As the number of oscillations has been kept constant for all central frequencies, the duration of the *voltage input pulses* T_i will decrease as $1/f_i$, (*Figure 4.10A)*. The bandwidth B_i of the pulse is defined in a similar manner to duration, *i.e.* the frequency range between the two half-amplitude points of the amplitude spectrum. This is inversely related to the duration through the uncertainty principle, which states that the product of bandwidth and

duration must be greater than or equal to 0.5 (Cohen, 1995). Hence the bandwidth of the *voltage input pulse* is proportional to frequency, *Figure 4.10B.*

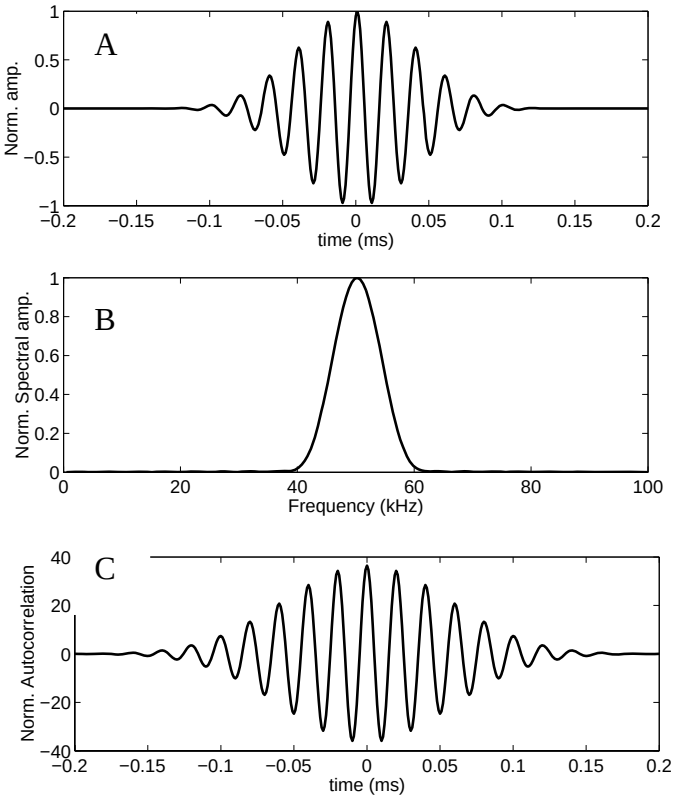

Figure 4.9. Properties of the voltage input pulse for a central frequency of 50 kHz including tonal pulse in time-domain (A), amplitude spectrum (B) and autocorrelation (C).

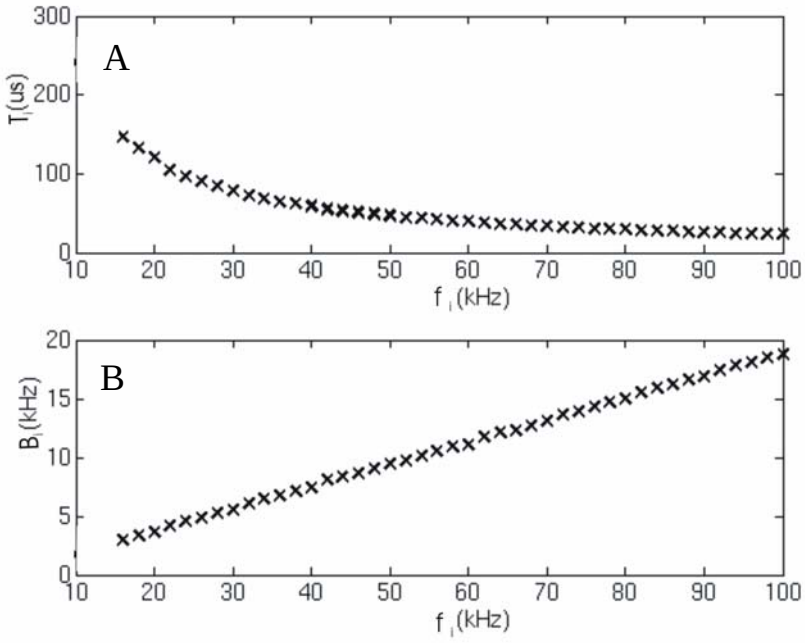

Figure 4.10. Variation of properties of voltage input signals with corresponding central frequency including duration T_i (A) and bandwidth B_i (B).

4.2.2. Properties of *voltage output pulse*

The properties of the *voltage output pulse* were obtained through the examination of four randomly selected sets of *voltage output pulses* recorded during the fieldwork, with five shots at each central frequency contained in each set. For central frequencies of 20, 50 and 100 kHz the overlay of the *voltage input pulse* and mean *voltage output pulse* are displayed, *Figure 4.11.* These have been normalised to maximum amplitudes of unity, by dividing by the corresponding maximum amplitude. The relative positions of the two pulses has been determined using a correlation of mean *voltage output pulse* with the corresponding *voltage input pulse*. If both pulses possessed exactly the same amplitude envelope and frequency content the overlaid pulses would be identical. Differences in location of less than half a period display the existence of small variations in the shape and/or frequency content of the input and output pulses, which result from frequency response of the source amplifier.

Over the lower central frequency range of 16 to 24 kHz the *voltage output pulse* possesses a tail which is absent from the *voltage input pulse*, *Figure 4.11A*, while 1st and 2nd harmonics, *i.e.* 40 and 60 kHz, can be observed on *Figure 4.11D.* The generation of harmonics arises from non-linear effects in the source amplifier, with “ringing” of the

source amplifier the most likely explanation for the extended tail. At frequencies greater than 24 kHz, both the magnitude of the harmonic components are negligible, *Figures 3.11E* and *3.11F,* and the magnitude of the tail is greatly reduced, *Figures 3.11B* and *3.11C.* The *voltage output pulse* and *voltage input pulse* resemble each other more closely at frequencies greater than 24 kHz than at those less than 24 kHz.

This displays the effective operational range of the amplifier. Pulses with central frequencies greater than 24 kHz lie well within this range. This reduces both ringing and non-linear effects, which result in the generation of a pulse tail and harmonic frequencies respectively, and results in a *voltage output pulse* that closely resembles the corresponding *voltage input pulse*. However, for central frequencies less than or equal to 24 kHz, the source amplifier is operating close to the bottom of the operational range, and hence the spectral and temporal envelopes of the *voltage output pulse* and *voltage input pulse* are observed to differ.

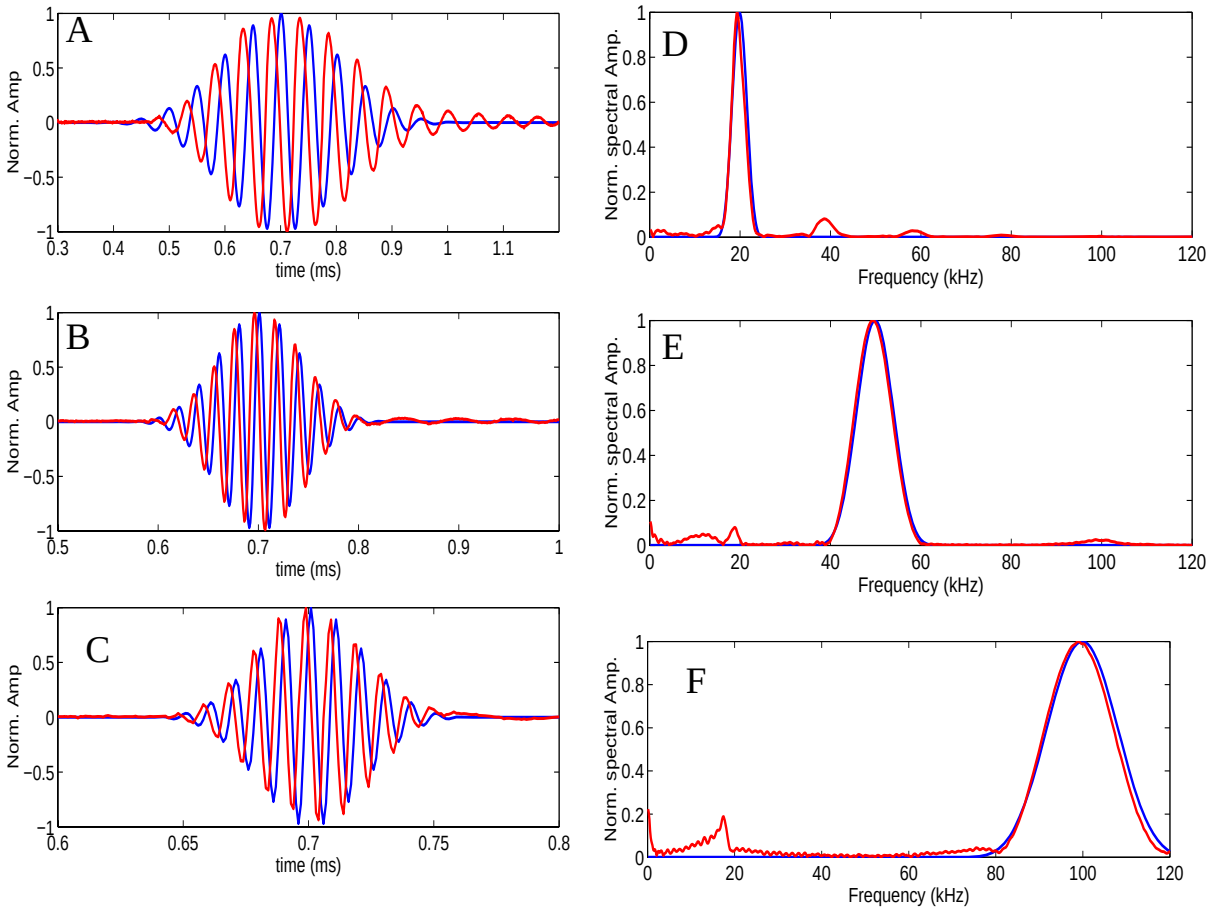

Figure 4.11. Comparison of voltage input pulses (blue) and typically voltage output (red). Includes pulses at: 20 kHz (A), 50 kHz (B) and 100 kHz (C) and spectra at 20 kHz (D), 50 kHz (E) and 100 kHz (F). Note varying time scale, to allow fine details of pulses to be observed.

The properties of the *voltage output pulse* are closely related to those of the *voltage input pulse*. They possess central frequencies f_o which are less than the input central frequency f_i, *Figure 4.12A*. These frequencies are linearly related through

$$f_o = 0.99 \cdot f_i - 0.17 \qquad 4.3,$$

where central frequencies are measured in kHz.

The durations T_o and bandwidths B_o of the voltage output pulse are displayed in *Figures 4.12B* and *4.13C* respectively. These follow the trends observed for the *voltage input pulse, i.e.* duration T_o varies with $1/f_i$, and bandwidth B_o is proportional to f_i . The bandwidths of the *voltage input pulses* and *voltage output pulses* differ by less than 1 kHz at any central frequency. However the durations T_o and T_i differ by between 30 and 125

μs, with the discrepancy more pronounced over the lower frequency range where ringing effects resulted in the generation of tails.

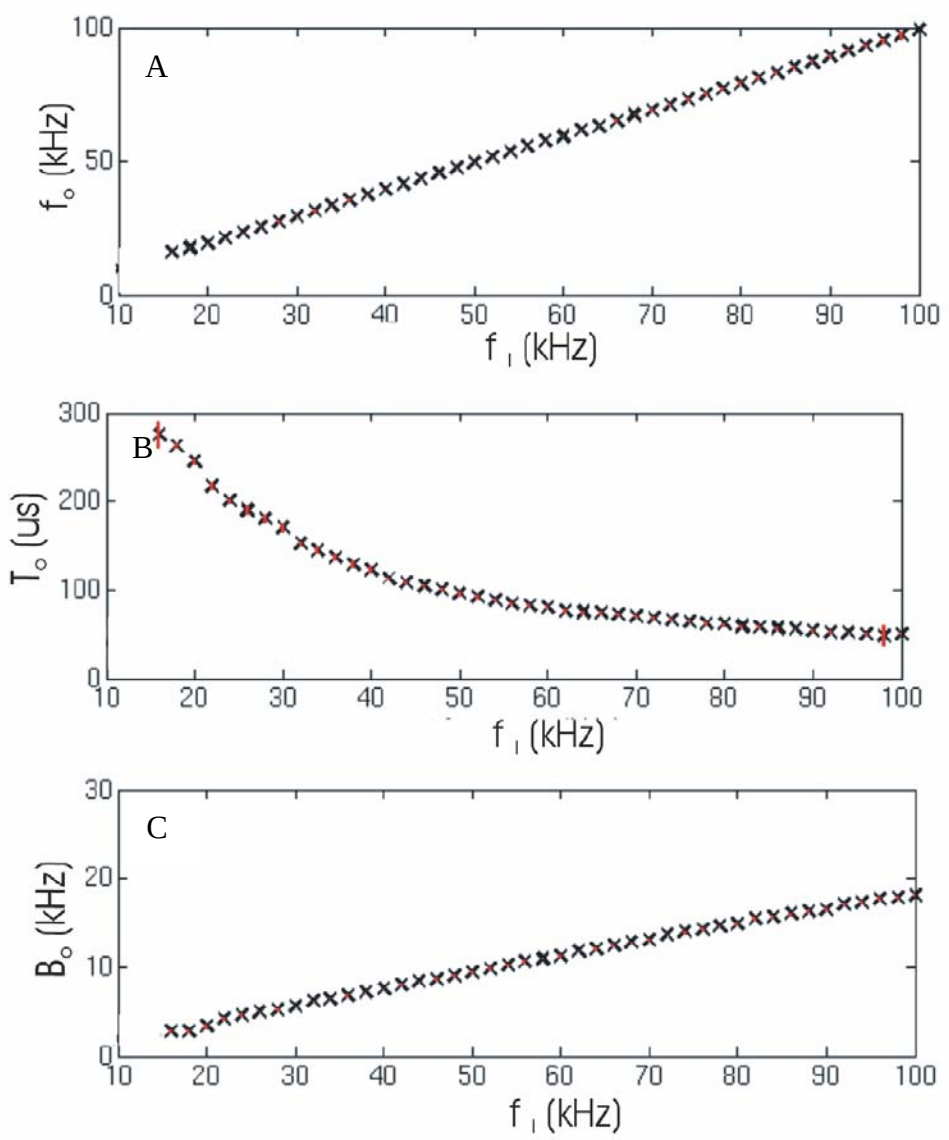

Figure 4.12. Mean properties of voltage output pulses including; mean central frequency f_o (A), duration T_o (B) and bandwidth B_o (C). Mean values are displayed by crosses, while standard deviations are denoted by red lines.

The amplitude of the *voltage output pulses* was measured using the mean voltage of each pulse. The use of the peak-to-peak voltage was extremely unreliable at higher frequencies, due to insufficient temporal resolution, *i.e*. at 100 kHz the sampling period of 1 μs corresponds to 10 % of the period. This was the maximum sampling frequency which

could be used to acquire the required length of received signal. The mean voltages, *Figure 4.13,* vary between 32 and 38 V, with the variation of mean voltage with central frequency incorporated by the processing techniques used to obtain attenuation coefficient (*Section 5.3.1).* Hence the important factor is the variability of the mean voltage at each central frequency, which is accurate to ± 5 % for all central frequencies.

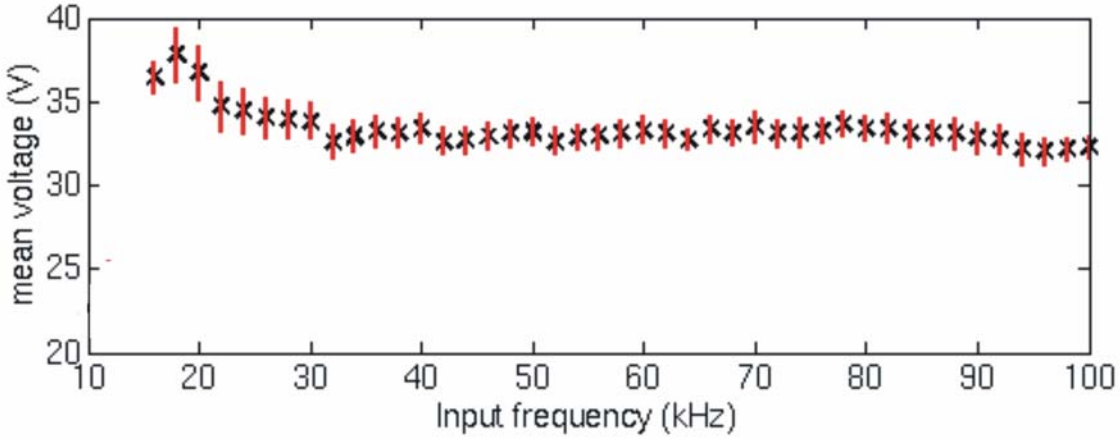

Figure 4.13. Mean voltage of voltage output pulses with mean values denoted by crosses and standard deviations by red lines. Values plotted are obtained from four randomly selected sets of voltage output pulses used during the fieldwork, with five shots present at each frequency in each set.

4.2.3. Properties of acoustic pulses transmitted through water

It is important to examine the properties of received pulses, which have propagated through water in order to determine the reliability of the acoustic wave emitted by the source and examine any changes in envelope resulting from the generation of the acoustic wave by the source transducer. Hence typical received signals which have been transmitted through 4.49 m of water are displayed in *Figure 4.14.* The water tests from which these signals were obtained are discussed in *Section 4.3.2,* while the pre-processing applied to the signal is discussed in *Section 5.1.* The corresponding *voltage output pulses,* which have been shifted by a time t_A (see *Section 5.2.3* for details) are also plotted. For all frequencies the discrepancies in the shape of the shifted *voltage output pulse* and the received pulse are negligible, with these pulses exactly overlaying each other at 50 kHz, *Figure 4.14B*. Hence for propagation through water the degree of distortion between the processed received pulse and processed *voltage output pulse* is negligible, the consequences of which are discussed in *Section 5.2.2.*

The repeatability of the acoustic wave propagated through water was also assessed through the examination of pulses with central frequencies of 20, 40, 60, 80 and 100 kHz at each of the receiver locations utilised in the water tests (see *Section 4.3.2* for details). For each receiver location and central frequency the five shots available were filtered to remove electronic noise. The temporal location of peak amplitudes of these pulses were repeatable to 1 μs and hence the acquisition system is reliable to 1 μs. The peak voltages, which were obtained from pulses extrapolated to a sampling frequency of 10 MHz to increase temporal resolution, varied from the mean peak voltages by less than 3.2 %. As this is less than the 5 % variability in the magnitude of the *voltage output pulse*, the source transducer and receiver do not introduce any further variability into the magnitude of the received pulse.

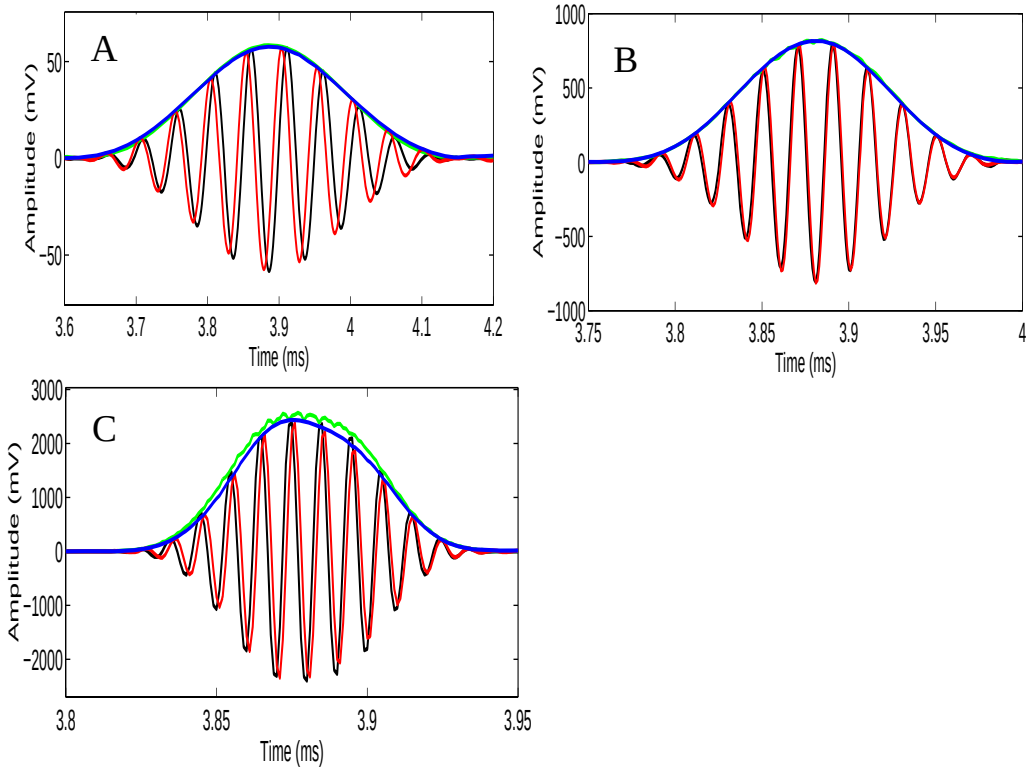

Figure 4.14. Typical received pulses detected during primary calibration tests at a S-R separation of 4.49 m, see Section 4.3.2 for details. Pulses are displayed for central frequencies of 20 kHz (A), 50 kHz (B) and 100 kHz (C). Note varying time axis to allow the fine details of the pulses to be displayed. The received pulse is denoted by the red line, with a blue envelope, and scaled and shifted voltage output pulse is denoted by the black line, with a green envelope.

4.3. Determination of pressure field emitted by the SPADE source

The technique developed in *Section 5.3* to measure the effective attenuation coefficient of marine sediments requires detailed knowledge of the pressure field emitted by the source. This pressure field will depend on the velocity of the medium through which the acoustic pulse is being propagated and will therefore vary from one sediment type to another. This factor has been neglected by a wide number of researchers, who either assume that spherical spreading losses are applicable (Fu *et al.*, 1996a; Lewis, 1971) or that spreading losses in the sediment and water are the same (Buckingham and Richardson, 2002; Hamilton, 1972; Shirley and Anderson, 1975). However, the use of incorrect spreading losses will result in incorrect estimates of effective attenuation coefficients.

Ideally a technique should be developed which would allow emitted pressure fields to be measured for each sediment type examined. As this would require pre-knowledge of the attenuation coefficient of the sediment, the measurement of which is the primary aim of this project, this is not possible. In addition all natural sediment possess some degree of heterogeneity, which will induce small-scale variations into the emitted pressure field. Therefore the approach adopted was to model the pressure field for a range of sediment types using a method which incorporated the velocity of the propagation medium, *Section 4.3.1*. The validity of the model was then confirmed through tests of the SPADE in a water tank, *Section 4.3.1*. Water was selected as a propagation medium owing to its truly homogeneous nature and its negligible attenuation of compressional waves over the frequency range of interest. Finally a variety of predicted pressure fields for velocities typical to saturated marine sands and silts were calculated, *Section 4.3.3.*

4.3.1. Modelling approach adopted

The approach adopted is a modified version of a technique used to predict the spreading losses of circular array transducers used in intravascular ultrasound imaging (Borsboom *et al.*, 2000). It is based on an impulse response method, which is implemented in the frequency domain.

The source was considered to be a section of a cylinder from which the sound radiates outwards, *Figure 4.15*. This geometry was an accurate representation of the shape of the SPADE source. The source was represented by the active surface S_p which was

surrounded by an infinite baffle. This was subdivided into a two-dimensional grid of small integration elements, the size of which must be "much less" than half the wavelength corresponding to the largest frequency in the radiated sound pulse (Borsboom *et al.*, 2000). The pressure *P(X,t)* at field-point *X* and time *t* can be obtained from

$$P(X,t) = \beta \int_{S} \int_{-\infty}^{\infty} \psi(t) \frac{\delta\left(t - t' - R/v\right)}{R} dt' dS \qquad 4.4,$$

where *t´* is a convolution time variable, β is a conversion constant, *v* is the compressional wave velocity, *R* is the distance between the field-point *X* and the surface element *dS*, $\delta(t)$ is a Dirac pulse and $\psi(t)$ is the impulse response of the transducer.

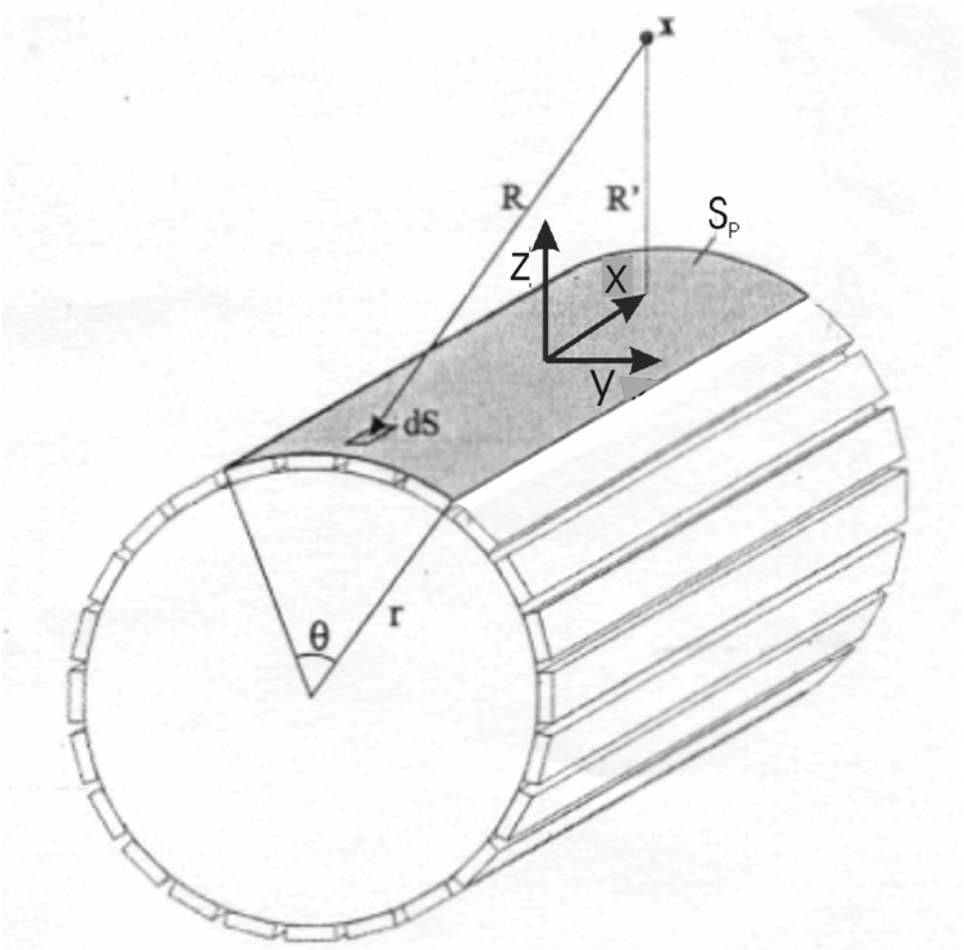

Figure 4.15. Geometry used in simulation program with active surface area of source denoted b shaded section S_p, from (Borsboom et al., 2000)

As only the relative variations in pressure were required, the conversion constant β could be set to unity. It was computationally advantageous to transform *Equation 4.4* to the frequency domain in order to simplify the convolution integral, which resulted in

$$P(X,\omega) = W(\omega)\int \frac{e^{-i\omega R/v}}{2\pi R} dS \qquad 4.5,$$

where $W(\omega)$ is the spectral amplitude at an angular frequency ω. This was computed using its discrete form

$$P(X,\omega) = W(\omega)dXdY\sum_{n=1}^{N_2}\sum_{m=1}^{N_3} \frac{e^{-i\omega R'/v} e^{-i\omega R_{n,m}/v}}{2\pi R_{n,m}} \qquad 4.6,$$

where N_2 and N_3 are the number of integration steps in each direction, dX and dY are the sizes of these steps, $R_{n,m}$ is the distance from element n,m to fieldpoint X and R' is the minimum distance between the point X and the transducer surface. The addition of the second exponential term removes the initial time offset for the first signal to arrive at field-point X. In order to prevent aliasing, the discretisation into frequency should be calculated in such a manner that all possible responses are accommodated, *i.e.* the pulse remains in the Fourier window.

The pressure response at a field-point X was obtained from the inverse Fourier Transform of $P(X,\omega)$, with the maximum value of the pressure response at each field-point X representing the emitted pressure field at that field-point.

As the impulse response of the transducer $\psi(t)$ was equivalent to the electronic pulse which was transmitted to the source transducer, *i.e.* the *voltage output pulse*, the spectral amplitude $W(\omega)$ was represented by the spectrum of this pulse. Hence, for each pulse used during the *in situ* experiments, *i.e.* pulses with central frequencies from 16 to 100 kHz in 2 kHz increments, a mean spectrum of the *voltage output pulse* was used for $W(\omega)$.

The parameters r and θ, *Figure 4.15,* which best define the SPADE source were measured to be 146 mm and 42.9^o (0.75 radians) respectively. Surface elements with a height of 2 mm and arc of 2 mm were used, which are less than 31 % of half of the the minimum wavelength examined, *i.e.* 6.5 mm. This just satisfied the condition stated earlier in this section that the size of the source element should be “much less” than half the minimum wavelength. The minimum wavelength was obtained from the maximum central

frequency, *i.e.* 100 kHz, and the minimum velocity, *i.e.* 1300 $m \cdot s^{-1}$, for which the pressure field was predicted.

Owing to the computationally demanding nature of the simulation program, care was taken to minimise the number of field-points used. The *in situ* fieldwork employed the SPADE source and receivers which were placed at the same depth. Hence the pressure field of primary interest lay in the horizontal plane which intercepted the centre of the source, *i.e.* the y-z plane indicated in *Figure 4.15.* In addition, only a reduced section of this plane was required. The grey shaded area in *Figure 4.16* incorporates all receiver locations used in the fieldwork. In order to examine the location of the near-to-far field transition sediment pressure fields were obtained for the entirety of the outer rectangle displayed in *Figure 4.16.*

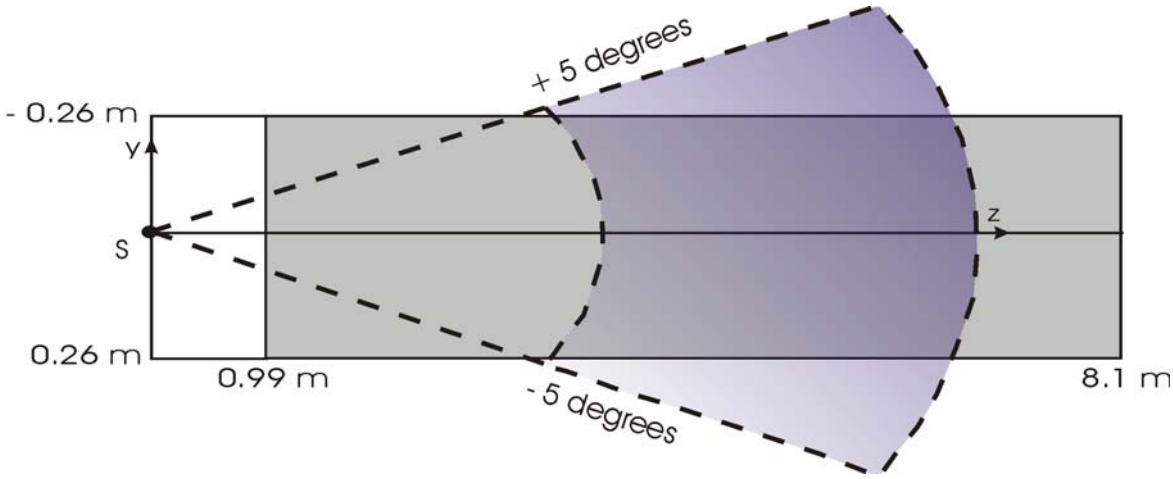

Figure 4.16. The shaded area displays the region containing all receiver locations used in the fieldwork, while the outer rectangle displays the region for which the pressure field was calculated, and purple arc displays regions spanned by primary acoustic tests.

The final stage was to select a suitable frequency discretisation, which must be sufficient to allow all possible responses to be accommodated. For a point *X*, which receives the start of the pulse from the element nearest to it at time t_o after the pulse has been emitted from the source, and the start of the pulse from the element furthest from it at time t_1 the Nyquist time required is calculated using

$$t_{ny} = (t_1 - t_o) + t_l \qquad 4.7,$$

where t_l is the length of the pulse, which is approximately ten oscillations at each frequency, as detailed in *Section 4.2.* The Nyquist time t_{ny} is related to the sampling frequency of the pulse f_s and the number of samples N_3 in the fast Fourier Transform (FFT) through

$$N_3 = 2 f_s \cdot t_{ny} \qquad 4.8.$$

For an efficient calculation it was desirable that $N_3=2^m$, where m is an integer. For the field-points required (*Figure 4.*16) the frequencies used (16 to 100 kHz) and a sampling frequency of 1 MHz (*Section 4.3*), a value of N_3 equal to 2048 was sufficient to allow all possible responses to be accommodated.

4.3.2. Verification of model

In order to validate the simulation program it was necessary to measure the pressure field emitted by the source in water. This involves measuring the amplitude of acoustic pulses which have propagated through a range of S-R separations and at a range of angles to the face of the source. These are used to measure the pressure field at a range of field-points, to which predicted pressure fields can be compared.

The primary acoustic tests were performed using the SPADE source and receiver in the AB Wood Tank, which is located on the Highfield Campus of Southampton University. This has a width of 8 m, length of 8m and depth of 5 m and permits a wide range of S-R separations to be examined. Secondary tests, which used a much more limited range of S-R separations, ranging from 0.5 m to 1.3 m, were undertaken by Drumgrange Ltd.

The primary acoustic tests are discussed first. *Figure 4.17* displays the locations of the SPADE source and receiver. The transducers were placed at a common depth of 2 m and in positions that were at least 1.4 m from the nearest wall. This prevented interference between the directly transmitted pulse and pulses reflected from either the water surface or the tank walls, with the clearly resolved nature of the received pulses displayed in *Figure 4.18.* The devices were positioned using scaffolding poles and S-R separation was measured to an accuracy of $\pm$ 2 cm, while depths were accurate to $\pm$ 1 cm. The well-constrained laboratory environment allow the angle of inclination of the devices to the vertical to be constrained to $\pm$ 1^o, while the relative angle in the horizontal between the faces of the source and receiver to be accurate to $\pm$ 2^o.

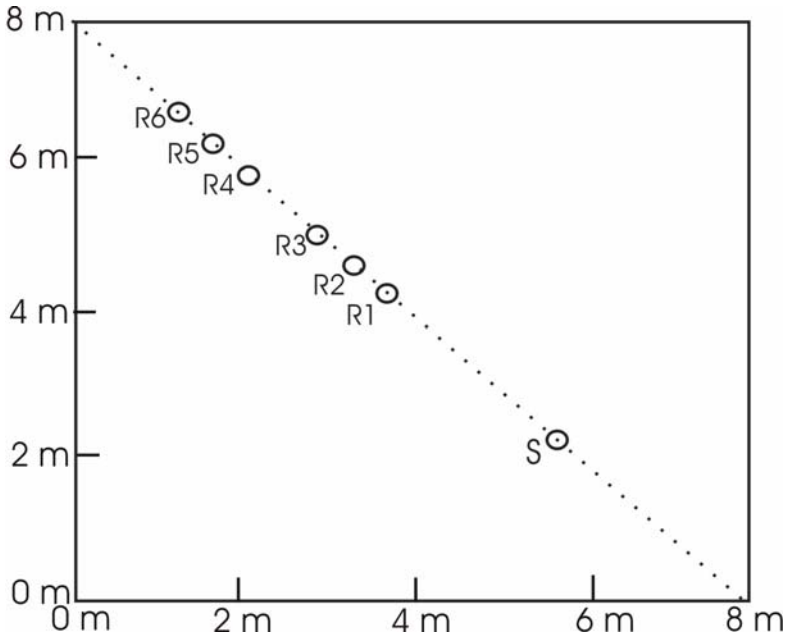

Figure 4.17. Plan view of positions of source and receiver in the water tank, with the outer square marking the perimeter of the tank.

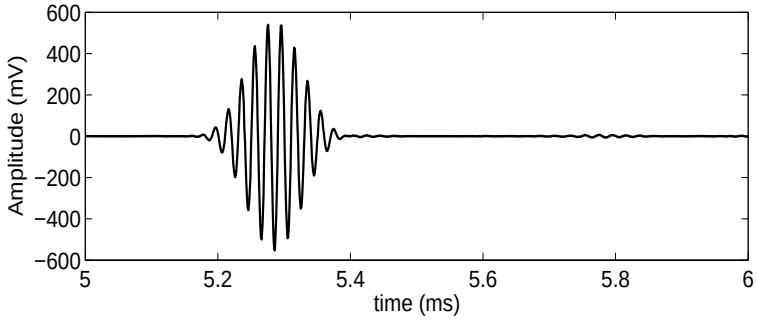

Figure 4.18. Typical signal received during the water test for S-R separation of 6.49 m and central frequency of 50 kHz.

The experimental procedure involved placing the source at position S and receiver at position R1, with a S-R separation of 3.49 m. The source was then rotated so that the receiver lay in a line perpendicular to the face of the source, *i.e.* 0^{o} from the centre of the emitted beam. Acoustic waves were then emitted and received, using five shots at each central frequency of 16 and 100 kHz, in 2 kHz steps. While frequencies between 16 and 70 kHz used the same source power settings as those used in the fieldwork, *Figure 4.13*, it was necessary to use a lower power setting to prevent signals with central frequencies between 72 and 100 kHz from clipping at the faces of the receivers. Hence, for a fixed voltage applied to the source transducer the amplitude of the acoustic wave emitted

increases as the central frequency of the pulse increases, which implies that the TVR of the source increases as frequency increases. The source was then rotated so that the receiver lay 5^o anticlockwise to the centre of the emitted beam (defined as + 5^o) and acoustic shots recorded. The source was then rotated so the receiver lay 5^o clockwise to the centre of the emitted beam (defined as – 5^o) and acoustic shots recorded. This entire procedure was repeated for receiver locations R2 to R6, with S-R separations of 3.99, 4.49, 5.49, 5.99 and 6.49 m respectively. In addition the temperature and salinity of the water was measured, resulting in a mean temperature of 16 ^{o}C, with a standard deviation of 0.6 ^{o}C, and a salinity of zero.

The region spanned by the primary acoustic tests is displayed in *Figure 4.16* as the purple shaded area. Though this does not encompass the relative locations of all receiver positions used during the *in situ* fieldwork, it represents the maximum degree of overlap that could be obtained (considering the dimensions of the AB wood tank and the amplitude of the acoustic wave emitted by the source).

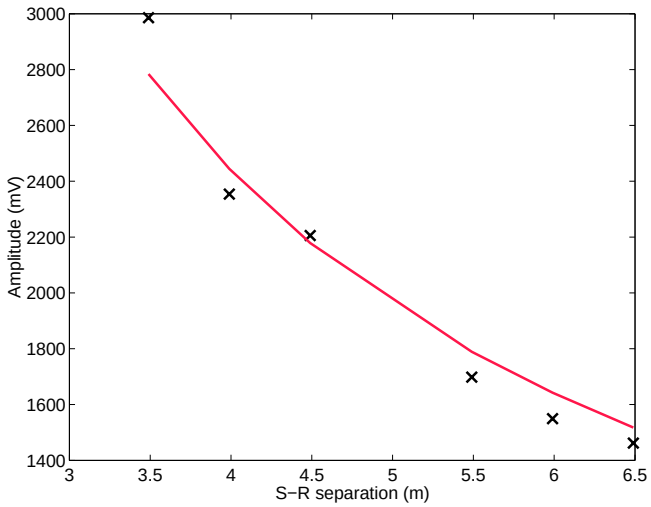

Figure 4.19. Amplitude versus S-R separation for the 0^o line and the 50 kHz pulse: crosses represents received amplitudes after attenuation of water has been removed and solid line displays the optimum fit of predicted pressure model.

The received pulses were processed using the technique described in *Chapter 5* to obtain the amplitude of the directly transmitted pulse. The intrinsic absorption of the water in dB·m^{-1} was calculated from the mean temperature and ranged from 6.6x10^{-5} dB·m^{-1} at 16 kHz to 2.6x10^{-3} dB·m^{-1} at 100 kHz (Schulkin *et al* 1962). Hence the absorption of the

water is negligible and the reduction of amplitude as the S-R separation increases is purely due to the spreading losses of the device. Typical results are displayed for the 0^o line at 50 kHz in *Figure 4.19.*

The predicted pressure field was then simulated using the following input values:

- A compressional wave velocity of 1470 $\pm$ 2 $m \cdot s^{-1}$. This was calculated from the salinity and temperature of the tank water using the empirical equations detailed in *Appendix A.*
- Field-points defined by a grid with *z* from 0.05 to 6.5 m in increments of 0.05 m, and *y* from – 0.6 to 0.6 m in increments of 0.02 m. This grid fully encompassed the region spanned by the primary acoustic tests, see *Figure 4.16,* with the relatively coarse nature necessary to allow for the computational demands of the program.
- The simulation was performed for each pulse used in the fieldwork, i.e. pulses with central frequencies from 16 to 100 kHz in 2 kHz steps.
- The predicted pressure field was then interpolated to a resolution of 0.01 m.

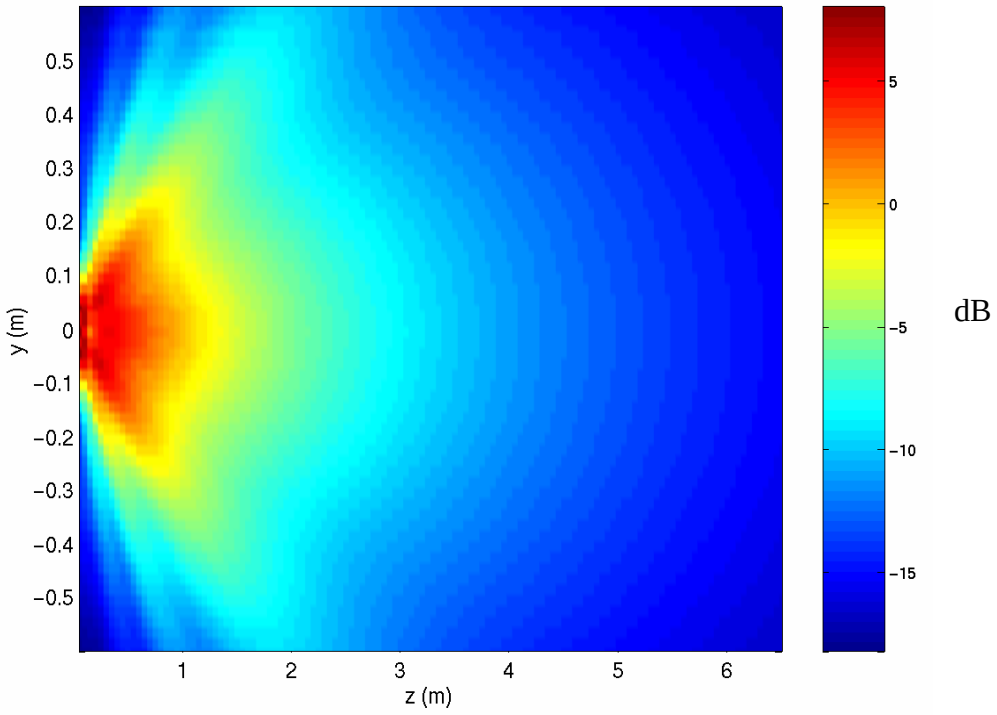

Figure 4.20. Predicted pressure field at a frequency of 60 kHz, in water with compressional wave velocity of 1470 $\pm$ 2 $m \cdot s^{-1}$. The field strength is expressed in dB relative to the reference point.

Figure 4.20 displays the predicted pressure field for 60 kHz. These pressure levels have been expressed in dB relative to the pressure at a point a distance 1 m from the source along the centre line of the emitted field, according to

$$dB(y,z) = -20 \cdot \log_{10}\left(\frac{P(y,z)}{P_o}\right) \qquad 4.9,$$

where $P(y,z)$ is the maximum amplitude at field-point $X(y,z)$ *(i.e.* the maximum value of the Inverse Fourier Transform of the spectral amplitude $P(X,\omega)$ in *Equation 4.6* and P_o is the maximum amplitude at the reference point. This is the reference point traditionally selected and will be used as the reference point for the remainder of the thesis. The 60 kHz results clearly display the presence of a main central lobe, with side lobes present for z>2 m.

The predicted pressure fields for water can now be compared to those measured by the primary acoustic tests. For each frequency and angle the six recorded amplitudes have been obtained, corresponding to the six S-R separations used. Corresponding predicted values, in dB relative to the reference point, are obtained from the predicted field. These predicted values are then scaled to produce a mean of zero and converted to predicted amplitudes through

$$A_P(y,z) = C_m \cdot \overline{A} \cdot 10^{-\frac{dB(y,z)-\overline{dB(y,z)}}{20}} \qquad 4.10,$$

where $A_p(y,z)$ is the predicted amplitude at field-point (y,z), $dB(y,z)$ represents the mean of the predicted values, $\bar{A}$ is the mean amplitude of the six measured amplitudes and C_m represents a scaling factor that ranges from 0.5 to 1.5 in steps of 10^{-3}.

The above approach is necessary as the TVR of the source is unknown and so the absolute values of the predicted pressure field is unknown. This allows the predicted and measured amplitudes to be aligned using their mean values. The scaling factor allows fine scale changes in the manner in which predicted and measured amplitudes vary with S-R separation to be incorporated. The value of C_m that produces the highest goodness of fit R^2 corresponds to the optimum fit between the predicted and measured pressure fields. The goodness of fit, R^2, represents the fraction of the total variance explained by the model and is computed from

$$R^2 = \frac{Var_T - Var_E}{Var_T} \qquad 4.11,$$

where Var_T is the total variance of the data and Var_E is variance of the data from the model. An example of a typical optimum fit is displayed in *Figure 4.19.*

Figures 4.21 to *4.23*, display the optimum values of R^2 and C_m for the - 5°, 0° and + 5° lines. The optimum values of the scaling constant range from 0.95 to 1. In the 0° and + 5° lines a step decrease is observed between 70 and 72 kHz, which agrees with the reduction in the source power for the frequency range of 72 to 100 kHz. The step increase in the optimum value of the scaling factor, which occurs between 70 and 72 kHz on the – 5° line is counterintuitive, the origin of which is unknown.

The resulting R^2 values vary from 0.79 to 1, representing a good to excellent fit. It can be seen that R^2 values reduce as frequency increases, indicating that the predicted pressure field is a better representation of the measured field at lower frequencies. The – 5° line displays a lower R^2 than the 0° and + 5° lines. This poorer degree of fit is consistent with the errors in the orientations and positions of the source and receiver (see details of primary acoustic tests earlier in this section).

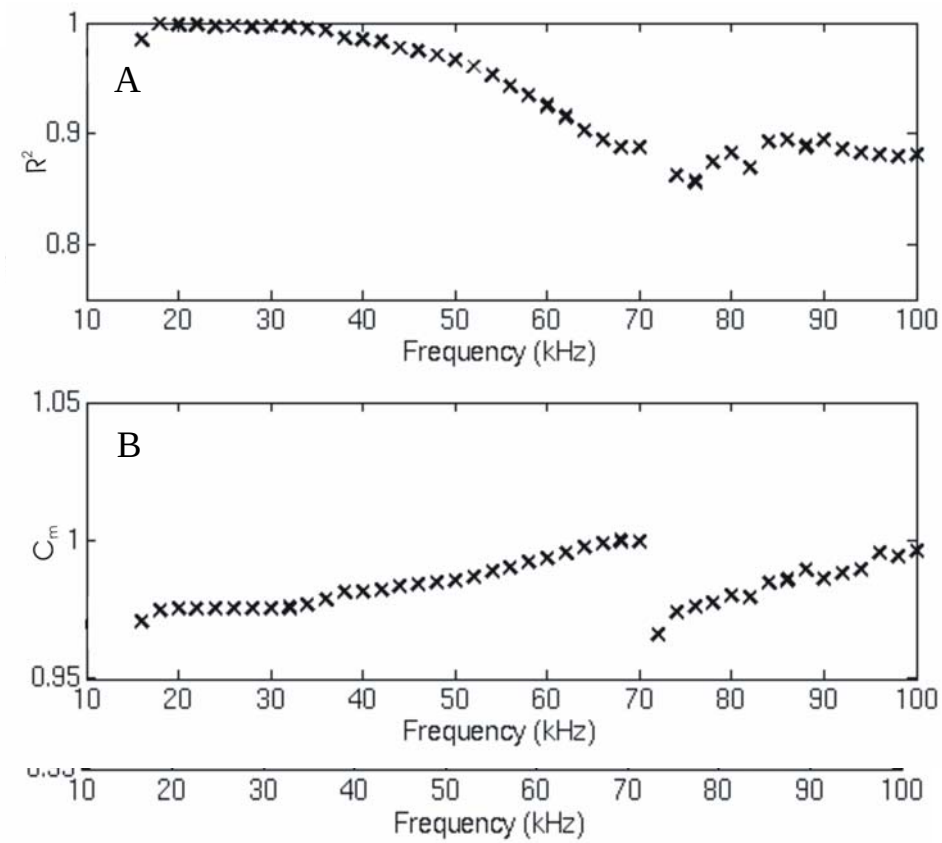

Figure 4.21. Goodness of fit R^2 and optimum scaling values C_m for – 5^o line.

Figure 4.22. Goodness of fit R^2 and optimum scaling values C_m for 0^o line.

Figure 4.23. Goodness of fit R^2 and optimum scaling values C_m for + 5^o line.

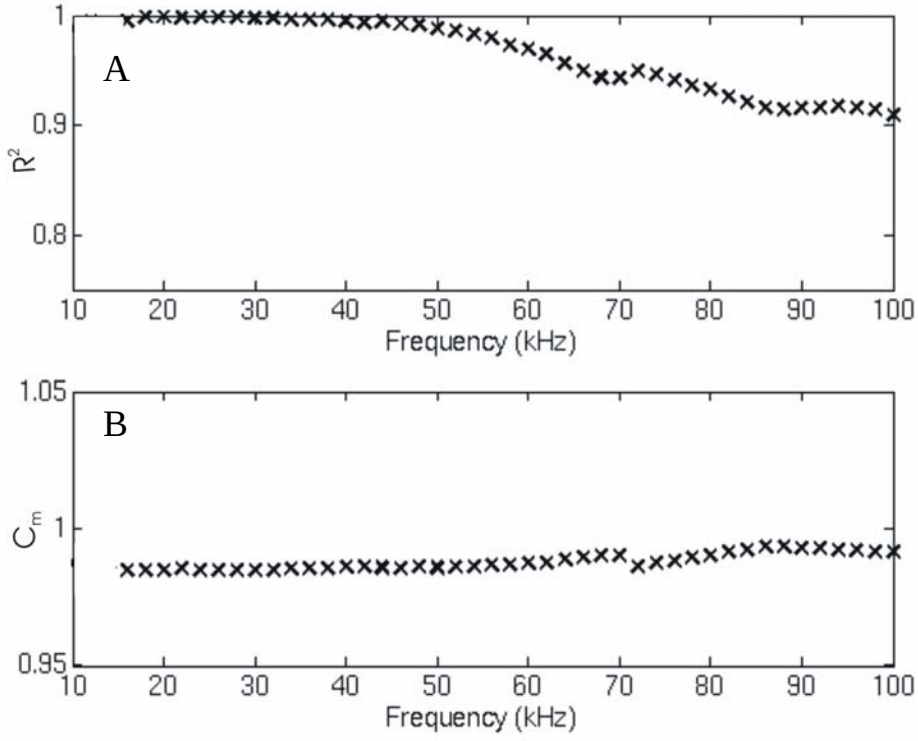

The acoustic tests, which were undertaken by Drumgrange Ltd., could only be used as a secondary check. This was due to the limited range of S-R separations used (0.5 to 1.3 m) which are a consequence of the equipment and tank used, and the lack of additional information, such as the electronic pulse applied to the SPADE source and the temperature of the water.

Pressure fields were measured using the SPADE source and a calibrated receiver. Rotation of the source through increments of 2^o allowed the beam pattern a fixed distance from the source to be measured. Beam patterns measured included:

- The beam pattern at a S-R separation of 1 m, spanning an arc of $\pm 55^o$ about the centre of the source, at frequencies of 20, 50 and 80 kHz.
- The beam pattern at 50 kHz spanning the full 360^o rotation at S-R separations of 0.5, 1 and 1.3 m.

For each of these six beam patterns, the only results available from the company were expressed in dB relative to the 0^o line which intersects the centre of the convex face of the source. The lack of any absolute pressures prevents the cross comparison of the six beam patterns measured, and hence all that can be achieved is a direct comparison between each measured beam pattern and that predicted by the simulation programme.

Figure 4.24 displays the results for the $\pm 55^o$ arcs at S-R separations of 1 m. The predicted beam pattern is obtained from the simulation model using the same velocity of water and field-points as detailed earlier in this section. The assumed range of water temperatures vary from 10 to 20 ^{o}C, which produces velocities from 1447 to 1482 $m \cdot s^{-1}$, see *Appendix 1* for details. Such variations in velocity will have a negligible effect on the predicted pressure field, *i.e.* differences were less 0.18 dB for all field-points and frequencies examined by the secondary tests. The effect of the unknown *voltage output pulse* applied to the source transducer during the secondary tests was examined by predicting pressure fields for both the tonal pulse used within this project, *Section 4.2*, and continuous waves. At a S-R separation of 1 m predicted beam patterns are only available for an arc of $\pm 37^o$, a consequence of the region over which the predicted pressure field was calculated, *Figure 4.16.*

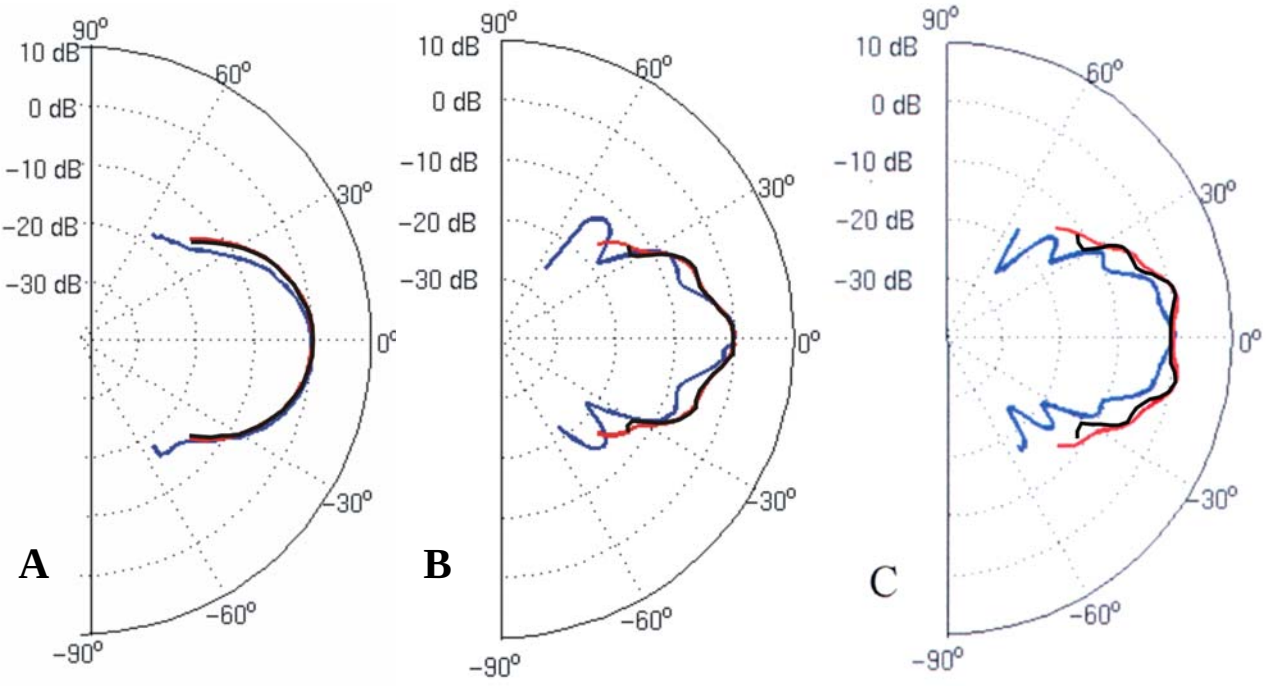

Figure 4.24. Comparison of measured beam pattern (blue) with those predicted for tonal pulses (red) and continuous wave (black) at a S-R separation of 1 m and frequencies of 20 kHz (A), 50 kHz (B) and 80 kHz (C). Results are expressed in dB relative to the 0° value.

The beam pattern predicted for a continuous wave agrees with the measured beam pattern better than that predicted for the tonal pulse, with the continuous wave case more accurately predicting the increased angular-dependence as frequency increases. At 20 kHz all beam patterns display the same omnidirectional nature, with the discrepancy between the measured and predicted patterns less than 1.74 dB and greatest for the larger positive angles. At 50 kHz the maximum discrepancy is 8.46 dB, while at 80 kHz the maximum discrepancy is 10.5 dB.

Figure 4.25 displays the results for the full 360° rotations at 50 kHz. For the S-R separations of 0.5, 1 and 1.3 m the predicted beam patterns are limited to arcs of $\pm$ 84°, $\pm$ 37° and $\pm$ 27° respectively. The measured patterns display much stronger angular dependences than the predicted beam patterns, with maximum discrepancies of 6.95, 7.8 and 3.0 dB for S-R separation of 0.5 m, 1 m and 1.3 m respectively. The beam patterns predicted for the continuous wave again provide better representations of the measured pattern than for the tonal pulse. As observed in *Figure 4.24*, the drop off with increasing angle is more pronounced in the measured pattern than in the predicted pattern. Though the magnitude of the beam emitted from the convex face is generally greater than that

emitted from the concave face, the magnitude of the central lobe emitted from the concave face is actually greater than or equal to that emitted by the convex face. This implies a back-front ratio of approximately unity.

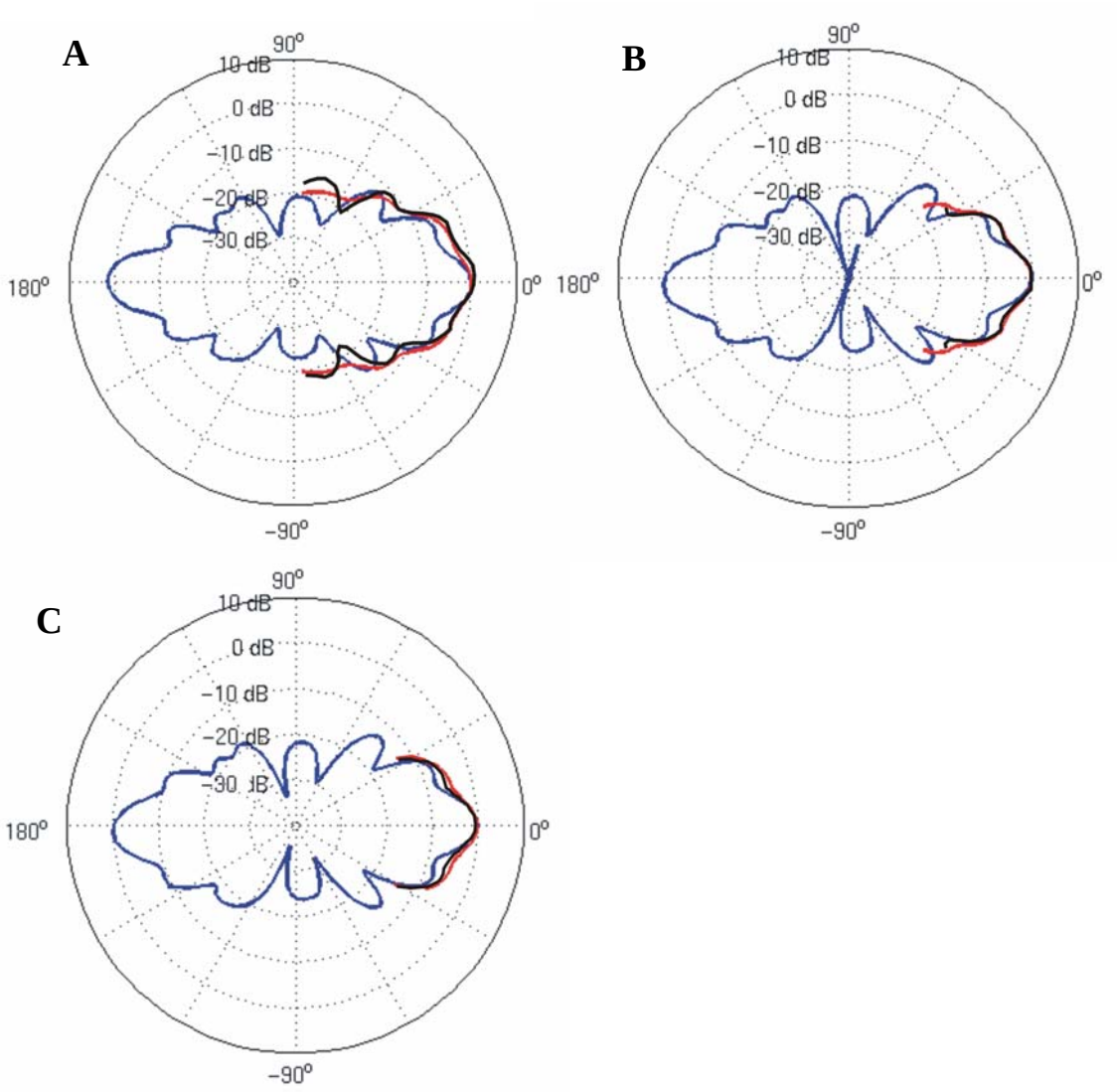

Figure 4.25. Comparison of measured beam pattern (blue) with those predicted for tonal pulses (red) and continuous wave (black) at a frequency of 50 kHz and S-R separations of 0.5 m (A), 1 m (B) and 1.3 m (C). Results are expressed in dB relative to the 0^o value.

The conclusion drawn is that the model adopted adequately predicts the pressure field emitted by the SPADE source for water. Agreement between measured and predicted fields are better for the more well constrained primary calibration tests, with increased

discrepancies with secondary tests primarily attributed to the unknown nature of the *voltage output pulse* applied to the source transducer. Hence it is concluded that the model used can be applied to any non-dispersive media with a known compressional wave velocity. The issue of whether marine sediments can be considered non-dispersive will be discussed in detail in *Section 6.1.*

4.3.3. Simulated pressure fields for typical marine sediments

The simulation program was used to determine the predicted pressure field in non-dispersive media with compressional wave velocities of 1300, 1400, 1500, 1600, 1700, and 1800 $m \cdot s^{-1}$. These values were selected as they span the range of compressional wave velocities observed at the range of inter-tidal sediments examined within this project (*Section 6.1*) with the lower velocities corresponding to silts and the higher velocities representative of sands. Predicted pressure fields were determined for grey shaded region in *Figure 4.16* and central frequencies of pulses used in the fieldwork, *i.e.* 16 kHz to 100 kHz in 2 kHz steps. *Figures 4.25* and *4.26*, display results for selected frequencies for a typical silt with a compressional wave velocity of 1400 $m \cdot s^{-1}$ and a typical sand with a compressional wave velocity of 1600 $m \cdot s^{-1}$.

For 20 kHz the pressure field is essentially omnidirectional at distances greater than 0.5 m from the source. As the frequency increases the size of the sidelobes become more dominant resulting in no central lobe at central frequencies of 80 and 100 kHz, for a velocity of 1400 $m \cdot s^{-1}$, and 100 kHz, for a velocity of 1600 $m \cdot s^{-1}$. Comparison of *Figure 4.26* with *4.27,* allows the effect of velocity on pressure field to be highlighted. The predicted field in the lower velocity medium possesses a greater angular dependence than the higher velocity medium does, which is especially clear at 80 and 100 kHz. The more unfocused nature of the emitted pressure field at higher frequencies is a consequence of the curvature and large surface area of the source. Though this may allow scattered signals from the sidelobes of the field to dominate over the directly transmitted signal, the ease of deployment and theoretical increase in the repeatability of the coupling between the source and the sediment outweigh this minor disadvantage and support the source geometry selected.

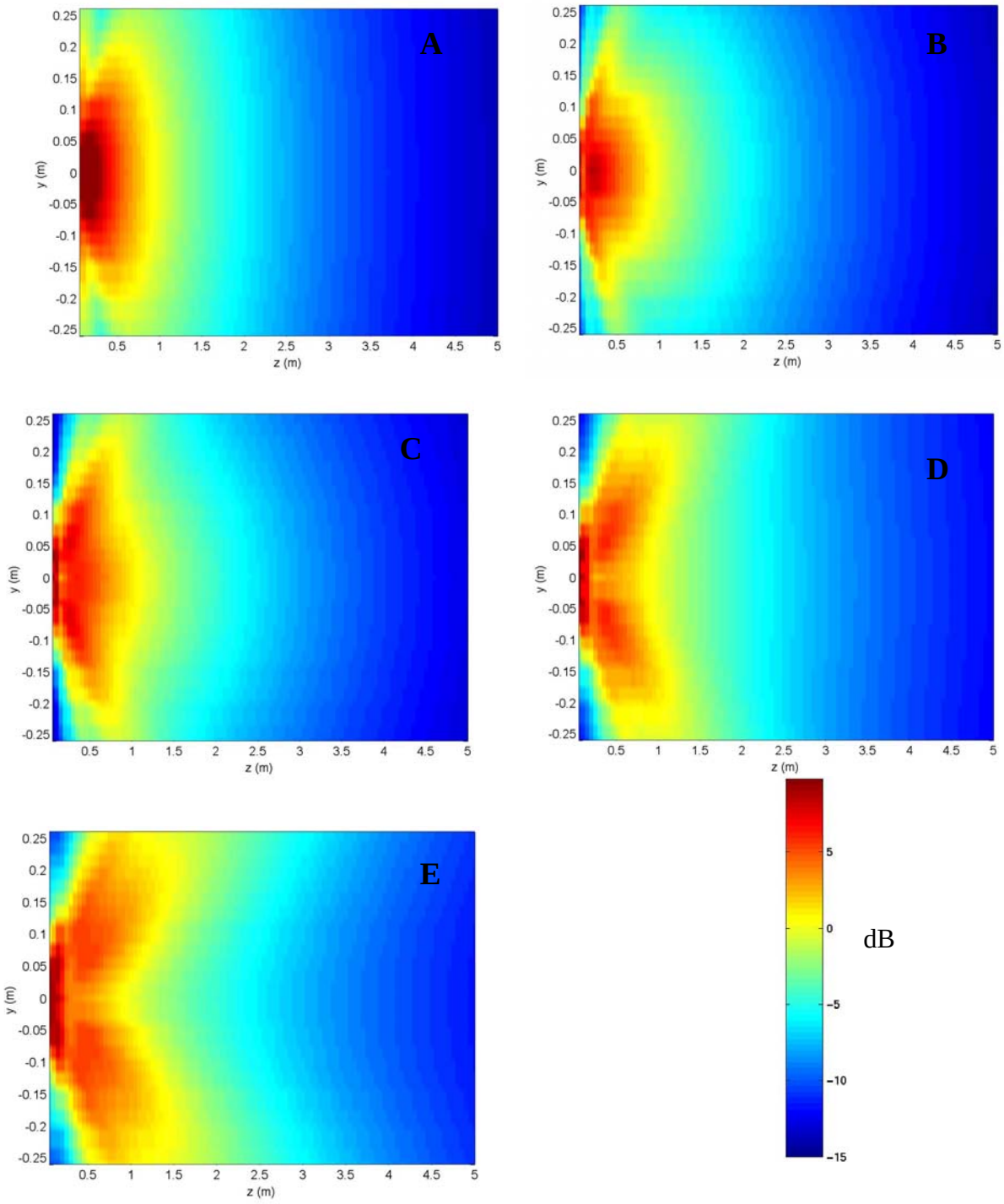

Figure 4.26. Zoom image of simulated pressure fields for a medium with a compressional wave velocity of 1400 m·s^{-1} (e.g. silt) and emitted pulses with central frequencies at 20 kHz (A), 40 kHz (B), 60 kHz (C), 80 kHz (D) and 100 kHz (E). The colour-bar displays the scale, in dB relative to reference point.

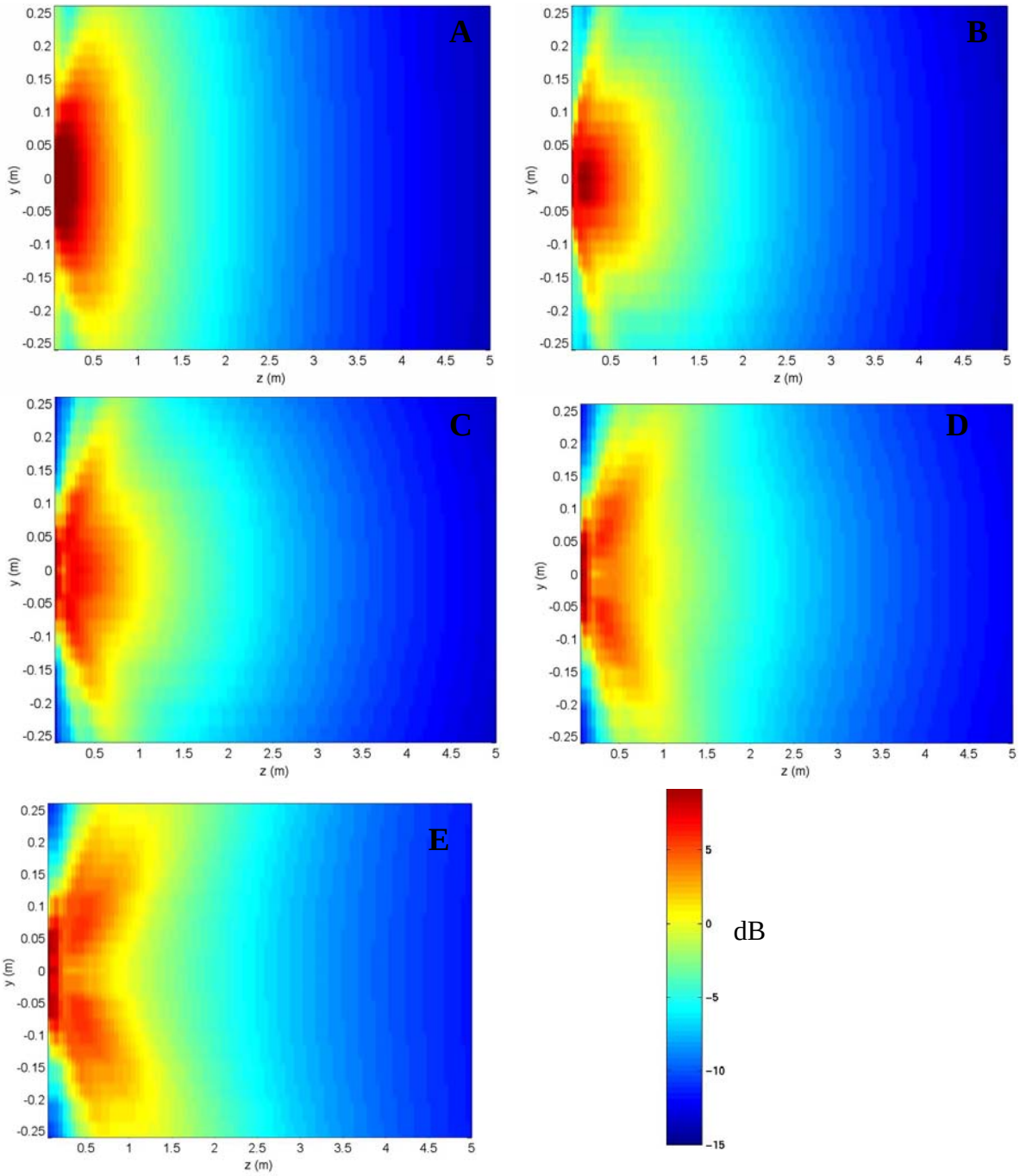

Figure 4.27. Zoom image of simulated pressure fields for a medium with a compressional wave velocity of 1600 m·s^{-1} (e.g. sand) and emitted pulses with central frequencies at 20 kHz (A), 40 kHz (B), 60 kHz (C), 80 kHz (D) and 100 kHz (E). The colour-bar displays the scale, in dB relative to reference point.

The predicted pressure fields can also be used to examine the distance from the source at which the near-to-far field transition occurs. In the near-field, the pressure field exhibits rapid spatial fluctuations due to a considerable degree of constructive and destructive interference. In the far field the pressure decays with $1/d^2$, where d represents the distance from the source, while the dependence of pressure on the angle to the source is reduced with respect to the near field.

The near-to-far field transition d_o can be estimated for a planar source from

$$d_o = \frac{H^2}{4\lambda} \qquad 4.12,$$

where H represents the height of the source transducer, which produces the larger near-to-far field transitions than the use of the width, and λ is the wavelength of the emitted wave (Leighton, 1994). Alternatively, the near-to-far field transition can be defined as the distance of the furthest pressure maximum from the source (Simpson *et al.*, 2002).

Figure 4.28 displays the variations in the pressure fields along the 0^o line from the centre of the source, at velocities of 1400 $m \cdot s^{-1}$, *Figure 4.28A,* and 1600 $m \cdot s^{-1}$, *Figure 4.28B.* As the central frequency increases, the near field region extends further from the source, with near field region extending as far as 0.45 m from the source at these velocities, and the steepness of the $1/d^2$ relationship observed in the far-field decreases.

Figure 4.29 displays selected cross-axis transects of the predicted pressure field along the line *z=1 m*. The dependence of the pressure field on the angle to the centre of the source is observed to vary with frequency and velocity. As the frequency increases the observed transects vary from a dominant central lobe at 20 and 40 kHz to dominant sidelobes at 80 and 100 kHz. As velocity increases, the dominance of the sidelobes becomes less pronounced. These observations are the consequence of an extended near field for higher frequencies and lower velocities.

The near-to-far field transition was measured using the furthest maximum from the source along the 0^o line for each frequency and velocity for which the emitted pressure field was predicted. If no maximum was observed the near-to-far field was placed at the minimum distance for which a pressure field was predicted, *i.e.* 5 cm from the source. The results are displayed in *Figure 4.30*, along with the transitions estimated from *Equation 4.12* for the maximum and minimum velocities of 1800 and 1300 $m \cdot s^{-1}$. The measured transitions increase as frequency increases over frequency ranges of 16 to 70 kHz and 90

to 100 kHz, which reflect the increased directionality of the emitted pressure fields observed in *Figures 4.26* and *4.27* as frequency increases. A null in transitions is observed from frequencies of 70 and 90 kHz, which are observed to correspond to the frequency range over which the shift from a dominant central lobe to dominant sidelobes occurs. As velocity increases the transition decreases, due to the wavelength of the emitted wave increasing with velocity.

The estimated transitions, which range from 0.05 to 0.48 m, again increase as frequency increases and velocity decreases. Though the estimated transitions generally agree with those measured, they are observed to be slightly less than those measured for frequencies of 25 to 70 kHz and slightly greater than those measured for 82 to 100 kHz. These discrepancies combine with the lack of a null in estimated transitions from 70 to 90 kHz to highlight that though the *Equation 4.12* obtains acceptable approximate values for near-to-far field transitions, its omission of the curvature of source transducer produces less accurate values than those obtained from modelled pressure fields.

The near-to-far field transition of the convex source obtained from the pressure model are deemed more reliable than those obtained from *Equation 4.12.* Hence, for all frequencies used and compressional wave velocities observed within the inter-tidal sediments examined the near-to-far field transitions occurs less than 0.45 m from the source.

Finally the difference between the pressure fields predicted for velocities of 1800 and 1300 $m \cdot s^{-1}$ and those predicted for water in the *Section* 4.3.2 were obtained for the grey shaded region in *Figure 4.16*, an example of which is displayed in *Figure 4.31.* For both velocities the difference in the pressure fields increased with central frequency, with a maximum difference of 2.5 dB for the higher velocity case (*i.e.* sands) and 1 dB for the lower velocity case (*i.e.* silts). These will result in corrections for spreading losses producing discrepancies in the amplitude of the received signal of 25 and 11 % respectively. Hence, the assumption that spreading losses in sediment and water are the same would have a considerable effect on the attenuation coefficient measured in both sands and silts.

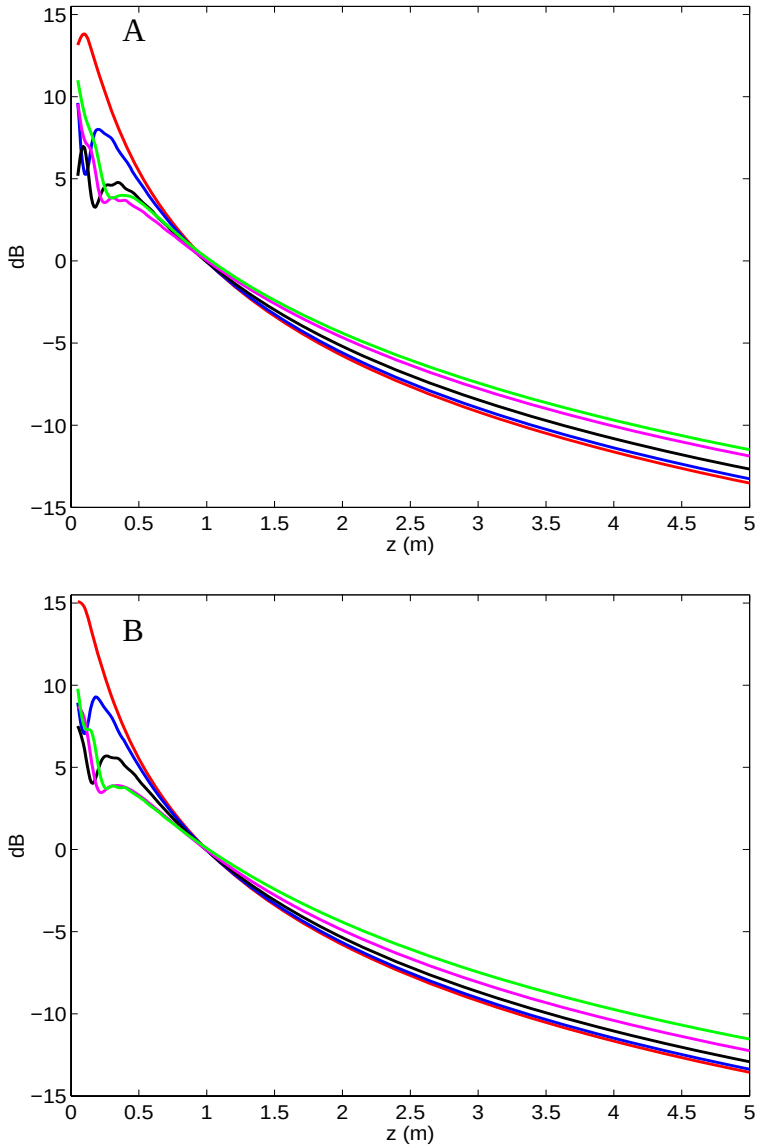

Figure 4.28. Transects of predicted pressured field along 0º line which intersect the centre of the source at frequencies of 20 kHz (red), 40 kHz (blue), 60 kHz (black), 80 kHz (magenta) and 100 kHz (green) and velocities of 1400 m·s^{-1} (A) and 1600 m·s^{-1} (B). Pressure fields are displayed in dB relative to the reference point.

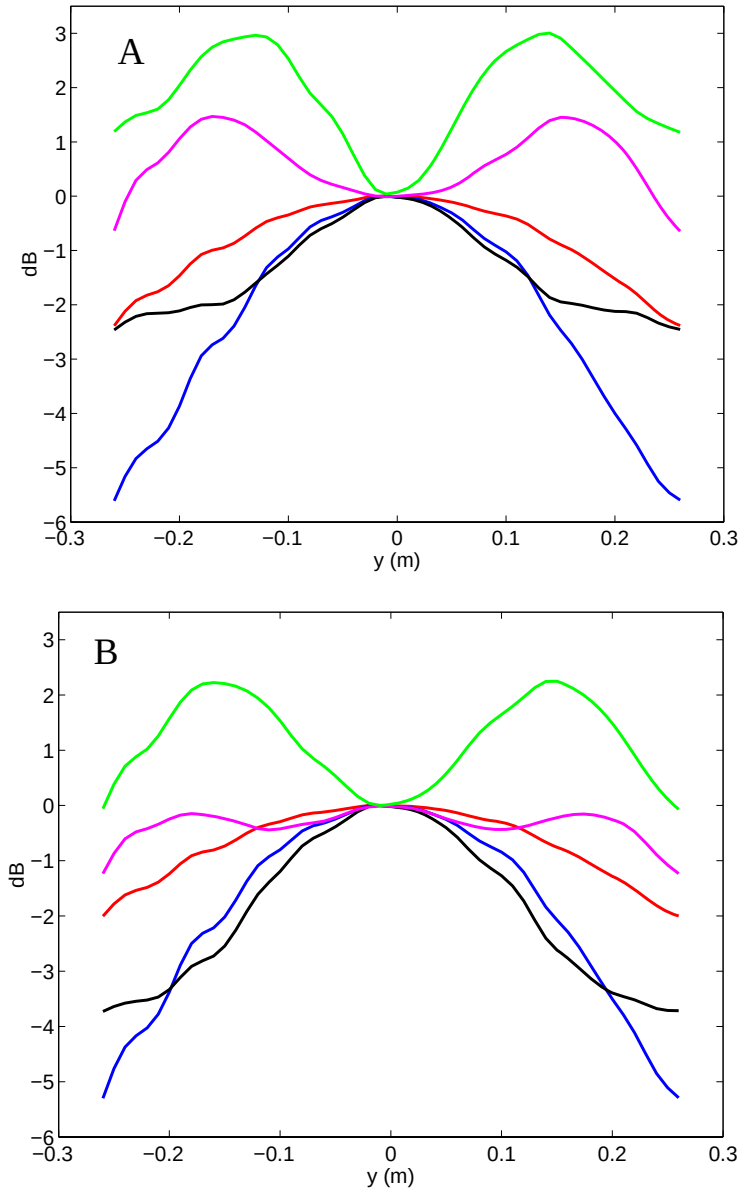

Figure 4.29. Transect of predicted pressure field corresponding to z=1 m, for frequencies of 20 kHz (red), 40 kHz (blue), 60 kHz (black), 80 kHz (magenta) and 100 kHz (green) and velocities of 1400 m·s^{-1} (A) and 1600 m·s^{-1} (B). Pressure fields are displayed in dB relative to the reference point.

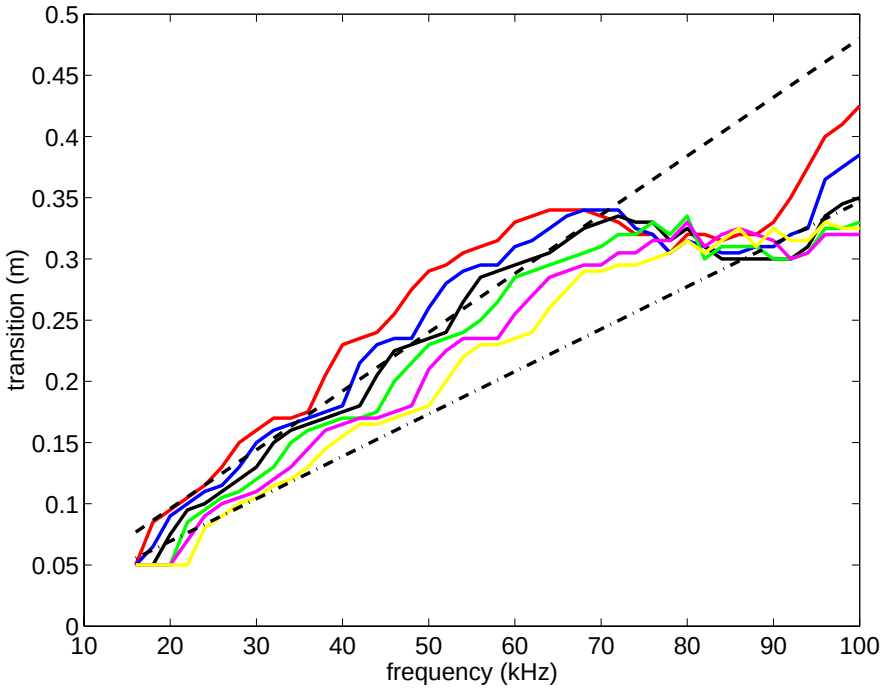

Figure 4.30. Near to far field transitions measured from predicted pressure fields at velocities of 1300 (red), 1400 (blue), 1500 (black), 1600 (green), 1700 (magenta) and 1800 $\mathrm{m \cdot s^{-1}}$ *(yellow). Estimated transitions obtained from Equation 4.12 are displayed for velocities of 1300* $m \cdot s^{-1}$ *(dashed line) and 1800* $\mathrm{m \cdot s^{-1}}$ *(dot-dash line).*

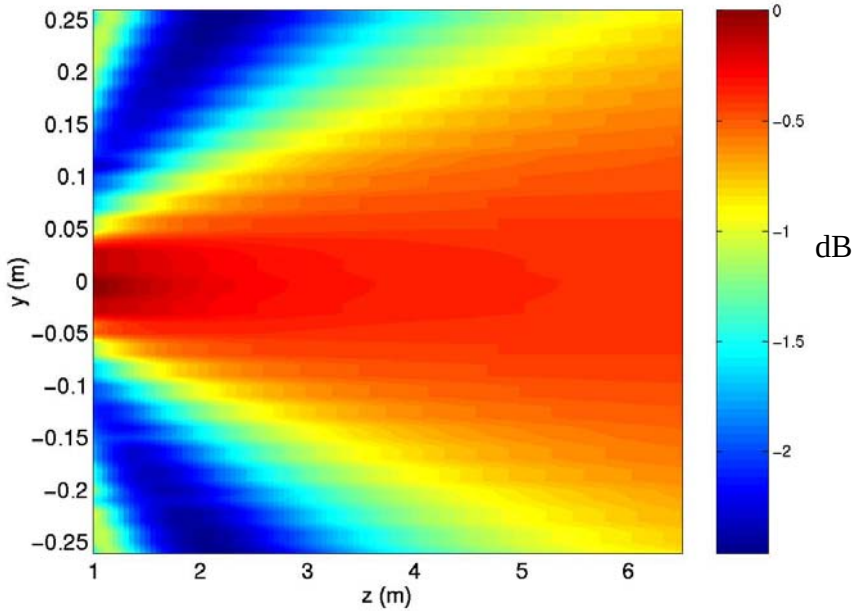

Figure 4.31. Difference between pressure fields predicted for compressional wave velocities typical to sand (1800 ms^{-1}*) and water (1470* ms^{-1}*), plotted in dB relative to reference point.*

4.4. *In situ* transmission Experiments

The SPADE was used in a suite of *in situ* transmission experiments which were performed on inter-tidal sediments, the methodology of which is discussed in *Section 4.4.1.* The details of the locations examined are discussed in *Section 4.4.2* and *4.4.3* respectively.

4.4.1. Methodology

The experimental procedure involved inserting the SPADE source and a pair of receivers vertically into inter-tidal marine sediment, with the inclination of the probes to the vertical accurate to $\pm$ 2^{o}. The centre of the source and receiving transducers were placed at a common depth of approximately 1 m ($\pm$ 0.02 m). A depth of 1 m will:

- Ensure that the sediment through which the acoustic pulses propagate is fully saturated.
- Reduce the possibility of any interference from reflections or refractions from the seabed surface.
- Allow sediment samples to be readily obtained from the sediment through which the acoustic wave propagates.

The two receivers were deployed, at approximately the same S-R separation, on either side of the central line of the field emitted by the source, *Figure 4.32*. The central line was defined by the line perpendicular to the face of the source. The S-R separation and offset distance, *Figure 4.33*, of each receiver were measured to an accuracy of $\pm$ 0.01 m.

The use of a pair of receivers increases the quantity of acoustic data which could be collected at each location examined. This is beneficial to the processing techniques used to obtain compressional wave properties, which are described in *Chapter 5.* The orientation of the receivers with respect to each other prevents reflected pulses from one receiver disrupting the signals detected by the other, while keeping the sediment volume examined to a minimum. The use of data from the two receivers at each S-R separation in the final analysis also acts to reduce the errors associated with coupling differences. Variable coupling has been highlighted by previous authors as a significant source of error (Buckingham and Richardson, 2002).

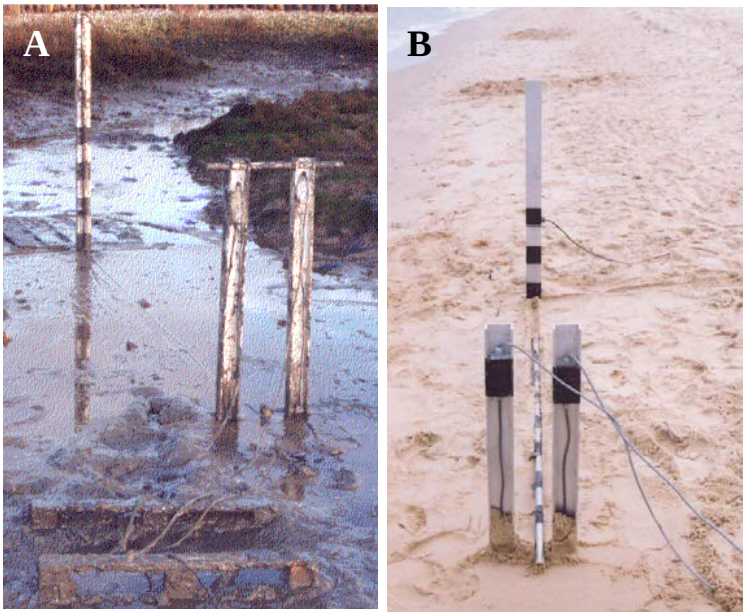

Figure 4.32. Probe deployments during fieldwork in a fine-grained sediment (A) and coarse-grained sediment (B). The receivers are located at approximately the same S-R separation, lying on either side of the central line, which is marked by the rope in (A) and measuring pole in (B).

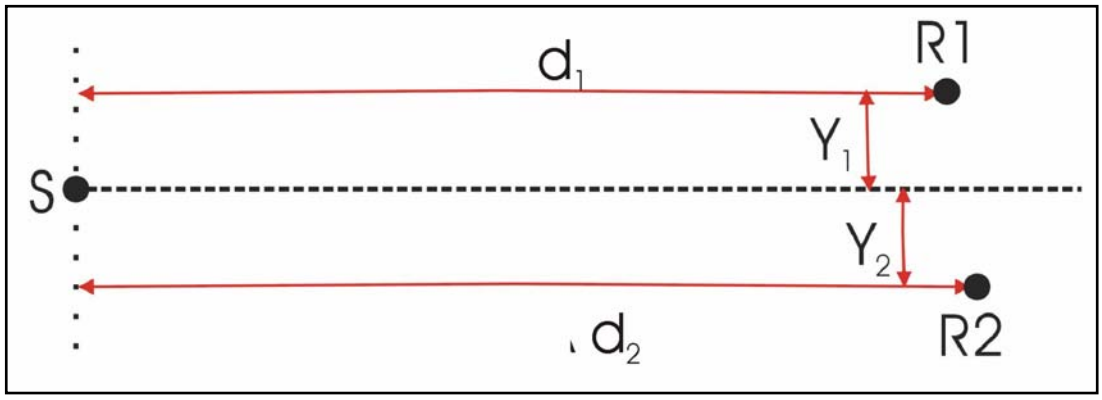

Figure 4.33. Distances used to measure the position of the receivers R1 and R2 relative to the source S. The S-R separations are defined as the perpendicular distance between the receiver and the line that runs parallel to and through the face of the source transducer. These are denoted by d_1 and d_2 respectively. The offsets are defined as the perpendicular distance from the receiver to the central line of the emitted field, denoted by Y_1 and Y_2 respectively. In order to clearly display the offsets the above diagram has been rescaled, with offsets used in the fieldwork ranging from 1 to 10 % of the S-R separations used.

The manner in which the probes were deployed differed for fine-grained and coarse-grained sediments. In fine-grained sediment, e.g. silts and clays, the devices could be forced straight into the sediment using body weight. This caused negligible disturbance of the sediment, hence ensuring that the properties measured truly represent the *in situ* properties.

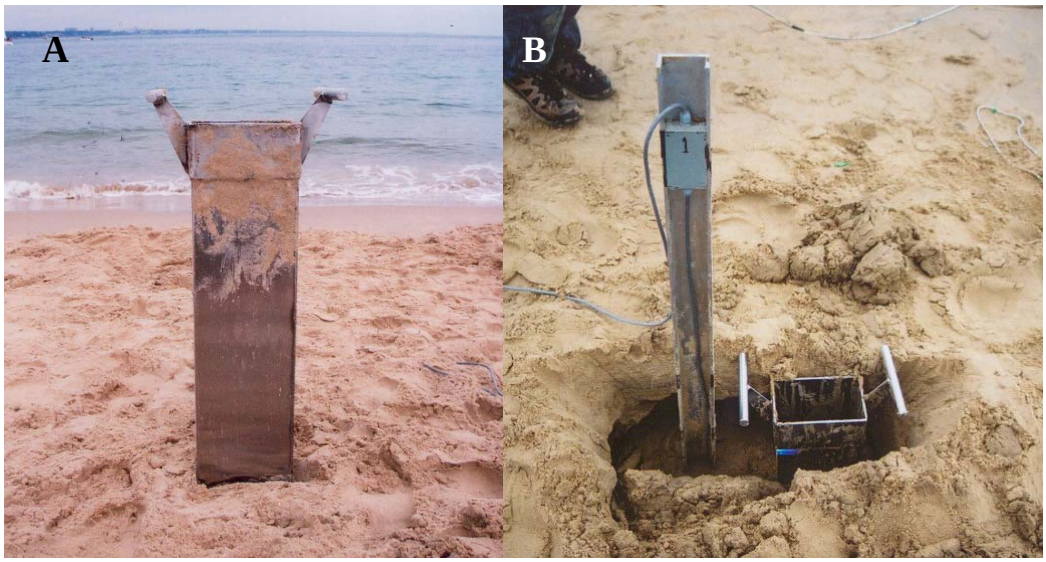

Figure 4.34. Deployment of device in coarse-grained sediment: (A) displays the insertion tool, while (B) displays its use mid deployment.

In coarser-grained sediments, e.g. sands, this method of deployment is not viable owing to the more compact nature of the sediment. It was necessary to develop an insertion tool (*Figure 4.34A)*. This resembled a box corer, with its width and breath modified to best fit the dimensions of the probes and two handles attached to aid insertion. The resulting dimensions of the tool, which was constructed from 1 mm thick stainless steel, were a height of 900 mm, width of 130 mm and breath of 210 mm. The upper 100 mm was strengthened to withstand the force exerted from the handles, by an additional band of stainless steel which was 4 mm thick. The method of deploying the source and receivers in coarse-grained sediments is displayed in *Figure 4.34B*. This involved digging a shallow hole, approximately 0.3 m deep, and using a rocking motion to force the insertion tool into the sediment to a depth of 1 m. The sand inside the insertion tool was then excavated manually and the required probe inserted into the cavity. The insertion device was removed and the remaining cavity filled. This technique permits the

deployment of the probes to the required depth, while minimising the sediment disruption caused, with the S-R separations of 0.99 m to 8.1 m used ensuring that the majority of the sediment through which the acoustic pulse propagates is undisturbed.

The acoustic pulses were then emitted from the source, detected by the receivers and recorded by the acquisition system. The pulses used consisted of 43 tonal pulses, with central frequencies from 16 to 100 kHz in 2 kHz steps. For each pair of receiver locations five shots of each of these pulses were emitted and recorded.

The receivers were then removed, redeployed at a closer S-R separation and the set of acoustic pulses described above re-emitted and recorded. It was important to move towards the source so that the sediment through which the pulses are propagating does not suffer any disturbance from previous receiver deployments. The increments of 2 kHz in central frequencies of the pulses emitted were selected in order to allow sufficient resolution to accurately examine the frequency-dependence of compressional wave velocity, attenuation and quality factor while allowing up to seven receiver deployments to be examined at each location. The range of S-R separations used varied from location to location in order to allow higher frequency signals to be detected above the background noise at larger S-R separations, while preventing the clipping of the lower frequency signals at smaller S-R separations.

Sediment samples were also collected for subsequent analysis. In the case of fine-grained sediments a thin “core” of sediment remained attached to the back of the aluminium channels on removal of the probe. A sediment sub-sample was collected from the portion of this “core” closest to the transducer. In the case of sands, the sample was obtained from the bottom of the insertion device during the excavation stage. At the sandy locations water samples were obtained from a depth of 1 m in the sediment and the sediment temperatures at this depth were measured. The alternative deployment techniques used in silts prevent water samples/temperatures being collected/measured at this depth, and hence surficial sediment temperatures were measured and water samples obtained from the neighbouring water body.

4.4.2. Details of fieldsites

Ideally the experimental procedure outlined above would have been performed on submerged seafloor sediments. However, with the SPADE in its present state of development, it can only be used to examine exposed sediments. This is due to the following factors. Firstly the manual method in which the probes are inserted into sands is only possible in exposed sediments. Secondly the length of the cables which attached the source amplifier to the source transducer were limited to 5 m, in order to minimise the resistance of the system and the power loss incurred.

A range of fieldsites were selected which satisfied the set of criteria below:

- The presence of a region of homogeneous inter-tidal sediment lying close to a point of good access. Whether a site was sufficiently homogeneous or not was determined though the excavation of a series of test holes over a lateral region of a few hundred metres. Sediment from each test hole was visually examined in order to observe if it belonged to the same sediment class and was vertically homogeneous, *i.e.* no clear sediment layering was present. The examination of a range of locations at each site will allow the effect of fine scale variations in geotechnical properties to be investigated.
- The region displayed a low tidal range. This ensured that sediment lying at a depth of 1 m did not drain as the tide ebbed, *i.e.* remained saturated throughout the entire tidal cycle. This condition was more critical for quickly draining sands, than for finer-grained silts which drained more slowly.
- The fieldsites were selected to encompass as wide a range of sediment types as possible, which will allow the dependence of compressional wave velocity, attenuation and quality factor on geotechnical properties to be investigated.

Figure 4.35 displays the co-tidal range of the South Coast of England, with contours representing the mean difference in tidal height between high and low tides. The co-tidal range possesses a minimum range less than 1.5 m in the proximity of Poole Harbour, which is located at 50^{o} 42’ N, 2^{o} W. Other regions in the British Isles which possess low tidal ranges include:

- Lowestoft, Norfolk, which possesses a co-tidal range of 2 m.
- Arklow, Co. Wicklow, Ireland, with a co-tidal range less than 1 m.
- Portrush, Co. Antrim, Northern Ireland, with a co-tidal range less than 1 m.

Poole Harbour was selected as the optimum region, due to its proximity to the research centre at which the project was based.

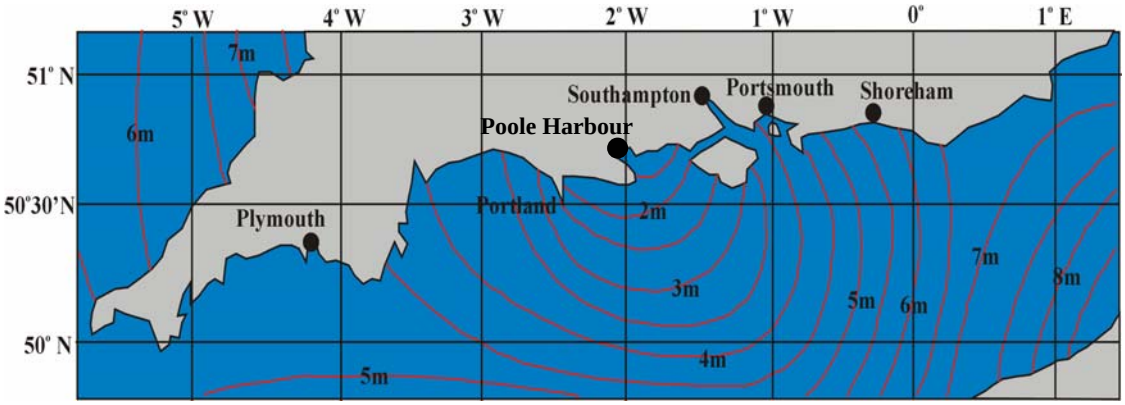

Figure 4.35. Co-tidal range of South coast of England.

Figures 4.35A to 4.34D display the location of the seven fieldsites selected. The three sites which possessed predominantly sandy sediment were located either in or at the mouth of Poole harbour. These are displayed in *Figure 4.35B* and are named Branksome, Studland and Lilliput after the surrounding areas. As no suitable sites which contained fine-grained sediments could be found in Poole harbour, the four sites which contained predominantly silty sediments were located on estuaries closer to Southampton. These included the Needs Ore site lying at the mouth of the Beaulieu River *(Figure 4.35C)*, and the Saltern, Universe and Mercury sites, which are located on the Hamble River (*Figure 4.35D)* and named after the neighbouring boatyards.

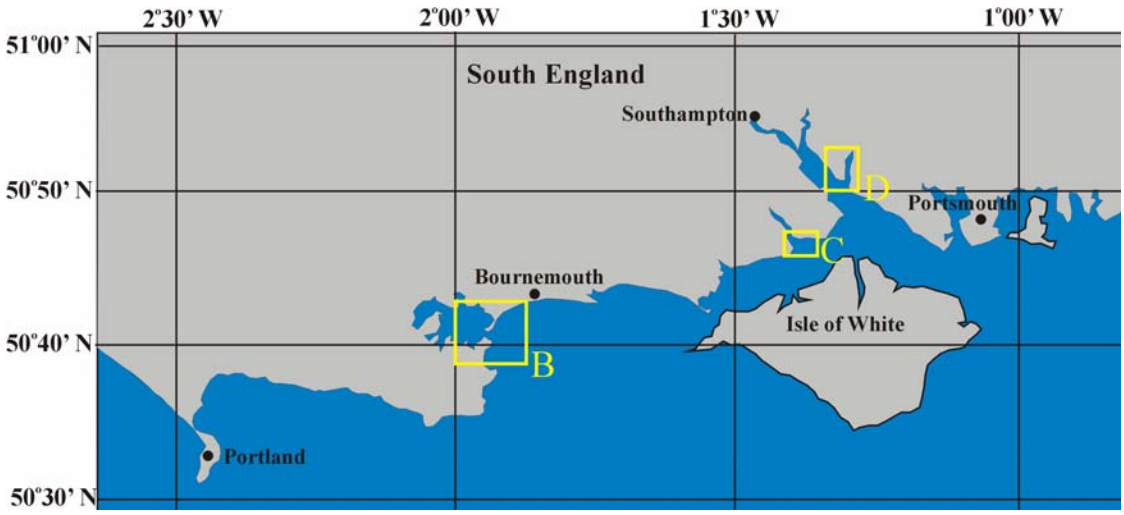

Figure 4.35A. Overall image of areas examined, with regions displayed in Figures 4.35.B to 4.35.D highlighted by yellow boxes.

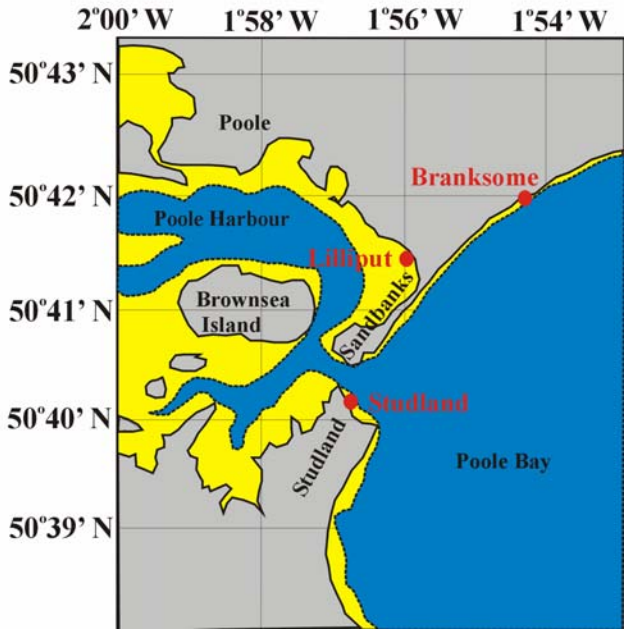

Figure 4.35B. Location of fieldsites examined in Poole Harbour. These included the Branksome, Lilliput and Studland sites, all of which possessed predominantly sandy sediment. Inter-tidal regions are denoted by yellow, while grey denotes land and blue denotes sea. Horizontal and vertical scales display latitude and longitude. Area displayed corresponds to region highlighted by box B in Figure 4.35A.

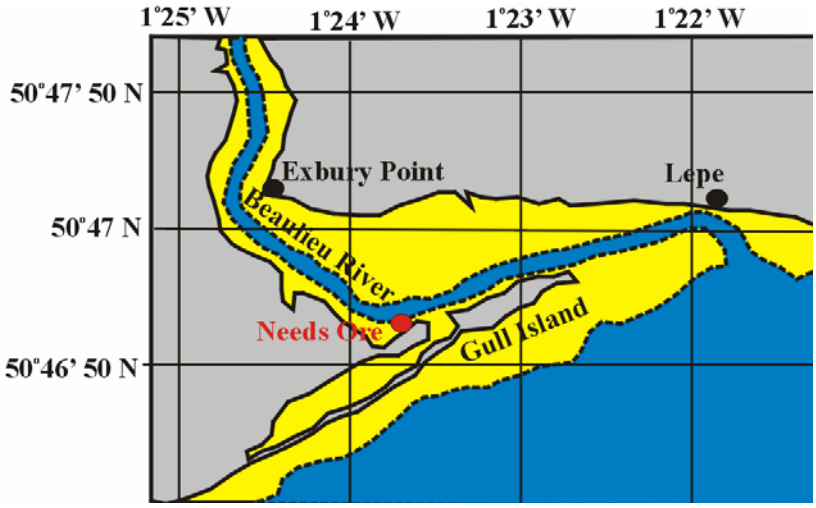

Figure 4.35C. Location of Needs Ore fieldsite, which possessed predominantly silty sediment. Inter-tidal regions are denoted by yellow, while grey denotes land, and blue denotes sea. Horizontal and vertical scales display latitude and longitude. Area displayed corresponds to region highlighted by box C in Figure 4.35A.

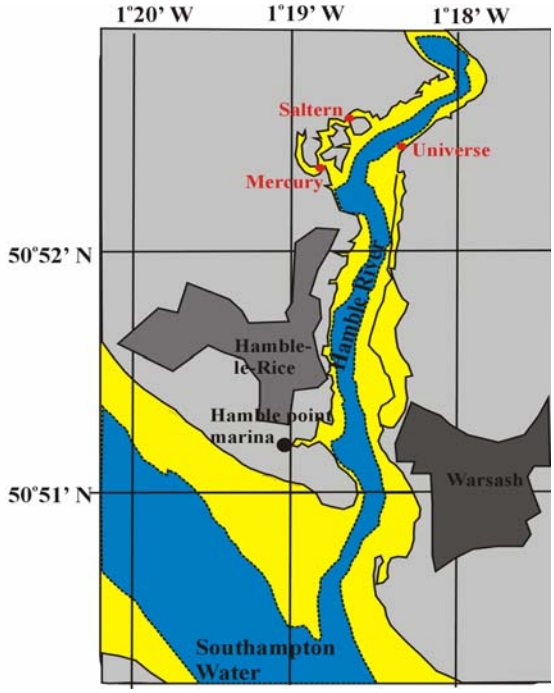

Figure 4.35D. Location of fieldsites examined in the Hamble River, which possessed predominantly silty sediment. Inter-tidal regions are denoted by yellow, while light grey denotes land, dark grey denotes villages and blue denotes sea. Horizontal and vertical scales display latitude and longitude. Area displayed corresponds to region highlighted by box D in Figure 4.35A.

Table 4.1 displays the details of these sites, including the number of specific locations examined at each general site, the number and range of S-R separations used and the observed saturation depth, with additional details included in *Appendix B.* The sites are broadly classified into sands (Studland, Branksome and Lilliput) and silts (Needs Ore, Mercury, Saltern and Universe) in *Section 4.4.3.* The saturation depth was measured as the approximate depth at which a water-table was observed. For all silt sites this was observed to lie less than 0.2 m below the sediment surface, which confirmed the slower-draining nature of the sediment.

All S-R separations used were greater than 0.45 m and hence all receiver locations lay in the far field. Though this was not strictly necessary, owing to the use of a pressure model (*Section 4.3)*, it reduced the error associated with the correction for spreading losses, see *Sections 5.3.1* and *5.3.3* for details. The range of S-R separations is generally greater in silts than sands, owing to the higher attenuation of compressional waves in sands, Exceptions occur for Lilliput 4, Mercury 1, Saltern 1 and 2 and Universe 1, with the reduced S-R separations in some of these silt sites attributed to the observation of heterogeneities which may cause additional energy losses (see *Appendix B)*. At all locations, bar two, between four and seven S-R separations were examined, with only three S-R separations examined at Studland 2, due to an electronic fault in the acquisition system, and Lilliput 2, due to an extremely short tidal window.

General Fieldsite	***Location examined***	***Range of S-R separations used (m)***	***Number of S-R Separations used***	***Saturation depth (m)***
Studland	1	1.24 – 1.94	5	0.5
	2	2.99 –3.99	3	0.3
	3	2.1-3.21	5	0.4
	4	1.79 – 3.03	6	0.5
Branksome	1	2.19 –3.21	6	0.6
	2	1.97 – 3.22	6	0.4
Lilliput	1	1.73 – 2.94	6	0.6
	2	2.53 – 2.98	3	0.7
	3	2.04 – 3.2	4	0.6
	4	4.17 – 7.39	6	0.5
Needs Ore Point	1	4.17 – 7.39	5	0.2
	2	2.94 – 5.92	6	0.2
	3	4.14 – 6.41	7	0.2
Mercury	1	1.06 – 1.95	5	0.2
	2	2.94 – 5.35	6	0.2
	4	5.0 – 7.37	5	0.2
Saltern	1	1.07 – 2.22	6	0.2
	2	1.25 – 3.19	5	0.2
Universe	1	0.99 – 2.94	5	0.2
	2	5.79 – 7.91	6	0.2

Table 4.1. Summary of fieldsites examined.

4.4.3. Geotechnical properties of fieldsites

At each location examined it is important that the properties of the pore water and sediment frame can be determined, in order to assess the effects of these properties on compressional wave properties.

The basic geotechnical properties measured at each location, using standard techniques which are detailed in *Appendix C,* include porosity n, bulk density ρ, mean

grain diameter M, sorting σ and percentage of sand sized particles. Porosity and bulk density were measured for one sediment sample from each location, while mean grain diameter, sorting and percentage of sand sized particles was measured for at least three samples at each location.

The sediments examined within this project fall into two main categories, medium to fine sands and medium to fine silts. The geotechnical properties of the sands are displayed in *Table 4.2*, and span the following ranges:

- Porosities from 39.5 to 55.3 %
- Bulk densities from 1789 to 2238 $kg \cdot m^{-3}$
- Mean grain diameters from 1.24 to 2.28 ϕ
- Percentages of sand sized particles from 97.6 to 99.9 %.

The geotechnical properties of the silts are displayed in *Table 4.3* and incorporate:

- Porosities from 75.9 to 92.7 %
- Bulk densities from 881 to 1169 $kg \cdot m^{-3}$
- Mean grain diameters from 6.22 to 7.89 ϕ
- Percentages of sand sized particles from 2.5 to 21.8 %.

The manner in which the intrinsic errors in the porosities and bulk density are obtained is outlined in *Appendix C.* Errors in porosity range from $\pm$ 0.23 to $\pm$ 1.05 % in sands and $\pm$ 4.41 to $\pm$ 6.96 % in silts, while errors in density vary from $\pm$ 12 to $\pm$ 41 $kg \cdot m^{-3}$ in sands and $\pm$ 56 to $\pm$ 81 $kg \cdot m^{-3}$ in silts. The increased errors in silts are a consequence of the smaller mass of sediment analysed with typical sand samples weighing approximately 1 kg and silt samples weighing approximately 100 g. This was a consequence of the different sampling techniques used in silts and sands, *Section 4.4.1.*

No intrinsic errors could be obtained for mean grain diameter, sorting or percentage of sand sized particles. Hence at each location the mean property obtained from the number of samples analysed was selected to represent the location, while standard deviations were selected as suitable errors. Resulting errors in mean grain diameter varied from $\pm$ 0.01 to $\pm$ 0.18 ϕ in sands and $\pm$ 0.05 to $\pm$ 0.72 ϕ in silts, while errors in percentage of sand size particles ranged from 0.03 to 2.78 % in sands and 0.13 % to 6.18 % in silts.

The relationship between the geotechnical properties measure in the laboratory and *in situ* values varies with the geotechnical property under consideration. Measured

properties that are based on grain size distributions, *e.g.* mean grain size, sorting and percentage of sand sized particles, will be identical to *in situ* values. As the manner in which the porosity was measured (*Appendix C*) does not preserve the sediment structure and measured values may differ from *in situ* values. In the case of sands, the settling of the sediment separates out the sand and silt particles, which would be mixed *in situ*. In the case of silts the requirement for a preliminary wet sieving destroys any sediment structure. Owing to the reduced consolidation effects in the laboratory than *in situ,* it is hypothesised that more open structures will be formed than present *in situ*, *i.e.* measured porosities will be greater than those *in situ,* while measured densities will be less than those *in situ.*

A more thorough examination of the errors in mean grain diameter allows the degree of homogeneity at each location to be assessed. Mean grain diameters and corresponding standard deviations for each location were converted to a maximum M_{max} and minimum M_{min} grain diameter in units of μm. The variability ΔM was then obtained from

$$\Delta M = 100 \cdot \frac{\left(M_{\max} - M_{\min}\right)}{\left(M_{\max} + M_{\min}\right)} \qquad 4.15.$$

Resulting values of sediment variability are displayed in *Tables 4.2* and *Tables 4.3.* For the sands these vary from 1.38 % to 12.41 %, while for all silts, except those at Mercury 2, a range of 4.15 % to 19.83 % is observed. These values represent the percentage by which the mean grain diameter varies across the sediment samples examined at each location. Hence the sands appear to be more homogeneous than the silts, with a reasonable degree of homogeneity observed for all locations examined bar one.

A further discussion of the variability would require detailed geological information about each site examined, such as the sedimentary layers present and dominant environmental processes. As the main thrust of this project is to determine how compressional wave properties depend on geotechnical properties and not a detailed geological examination of sediment variability, this was not undertaken.

Location	Description	n (%)	ρ ($kg \cdot m^{-3}$)	M (ϕ)	σ (ϕ)	Sand Fraction (%)	ΔM (%)
Studland 1	Bimodal Moderately well sorted medium sand	-	-	1.24	0.66	-	12.41
Studland 2		55.3	2238.8	1.94	0.62	99.84	3.46
Studland 3		39.5	1960.7	1.79	0.60	99.9	6.92
Studland 4		39.1	1978.0	1.95	0.75	99.54	9.67
Branksome 1	Unimodal well sorted medium sand	40.3	1973.5	1.70	0.40	99.52	4.36
Branksome 2		40.2	1967.1	1.97	0.49	99.98	1.38
Lilliput1	Unimodal well sorted fine sand	50.7	1789.2	2.18	0.40	99.34	5.54
Lilliput 2		51.2	1971.4	2.28	0.50	97.65	12.41
Lilliput 3		42.6	1835.9	2.15	0.48	98.77	7.61
Lilliput 4		46.2	1805.7	2.18	0.43	98.91	3.46

Table 4.2. Geotechnical properties of locations examined which possessed predominantly sandy sediments.

Location	Description	n (%)	ρ ($kg \cdot m^{-3}$)	M (ϕ)	σ (ϕ)	Sand Fraction (%)	ΔM (%)
Needs Ore 1	Unimodal Poorly sorted fine silt	82.0	1102.5	6.56	1.64	9.14	17.83
Needs Ore 2		89.9	1155.9	7.89	1.70	8.59	19.83
Needs ore 3		91.9	1143.9	6.78	1.58	9.10	14.45
Mercury 1	Unimodal Poorly sorted fine silt	90.9	1085.5	6.70	1.64	12.05	6.69
Mercury 2		84.5	1138.1	7.20	1.69	3.23	46.14
Mercury 3		88.3	1107.8	6.96	1.73	2.48	4.15
Saltern 1	Unimodal Poorly sorted medium silt	92.5	1169.5	6.65	1.48	12.65	17.15
Saltern 2		92.7	1122.3	6.89	1.67	6.09	12.41
Universe 1	Unimodal Poorly sorted medium silt	75.9	881.3	6.22	1.33	12.64	6.92
Universe 2		90.2	1038.9	6.26	1.87	6.09	15.13

Table 4.3. Geotechnical properties of locations examined which possessed predominantly silty sediments.

Some cautionary notes shall be made concerning the measured values of mean grain size and sand fraction. Firstly some of the grain size distributions were bimodal, an example of which is displayed in *Figure C.3.* In such cases the mean grain diameter does not accurately represent the dominant, or modal, grain diameter. This was taken into consideration when the dependence of compressional wave properties on mean grain diameter were examined, *Section 6.2.3*. Secondly, the sand sized fraction of the silts are

dominated by organic material, and contain very few actual quartz grains. Thirdly, the analysis of the mud fraction should yield a maximum grain diameter of 63 μm, as all particles greater than this have been removed by wet sieving the samples. However, some particles were observed with dimensions greater than this, *Figure C.5,* which is probably due to flocculation of smaller particles to form larger ones despite the addition of deflocculant, *Appendix 3.* Across all silts samples examined, less than 6.4 % of the total volume possessed grain diameters greater than 63 μm, hence the effects of this discrepancy will be negligible.

At each location, the temperature of the sediment was recorded and water samples were collected, either from the pore water or from surface water. Salinity was obtained from these samples using a standard salinity probe. The resulting upper and lower limits of salinity and temperature are displayed in *Table 4.1.* Salinities are lower than those observed for typical marine environments, which range from 33 to 37 ‰ in open sea surface waters *(Brown et al 1995)*, owing to the estuarine and inter-tidal nature of the sites examined. Temperatures are noticeable lower for the sites containing silts than those containing sands, due to the examination of sandy sites from July to October and the examination of silty sites from November to December (see *Appendix B)*. It is assumed that the salinities and temperature of the surface water and the pore water lying 1 m below the surface at the silty sites examined are the same.

Site	Temperature (^{o}C)	Salinity (‰)
Sands	14.0 – 18.0	0.3 – 6.3
Silts	2.5 – 14.5	0.3 - 4.1

Table 4.4. Range of temperatures and salinities measured at sand and silt sites.

Finally the values of and inter-relationships between the geotechnical properties measured will be compared to those observed in the literature (Hamilton, 1987). Though this is not the primary aim of this project such a comparison will improve the understanding of the inter-tidal sediment under examination. The results from the literature, *Table 4.5,* have been corrected to laboratory conditions, and are obtained from samples in the upper 30 cm of the seafloor, lying at water depths of hundreds to thousands

of metres. Values have been selected for continental shelf sediments, which display a similar range of grain diameters to those observed in the sand and silt groups examined within this project.

Sediment	M (ϕ)	n (%)	ρ ($kg \cdot m^{-3}$)	Sand fraction (%)
Coarse to fine sand	0.92 – 2.62 (1.24 – 2.28)	38.6 – 44.5 (39.1 – 55.3)	1962 – 2034 (1789 – 2239)	92.2 – 100.0 (97.6 – 99.9)
Sand-silt-clay to silty-clay	5.82 – 8.80 (6.22 – 7.89)	66.3 – 73.0 (75.9 – 92.7)	1480 – 1575 (881 – 1169)	3.9 - 31.7 (2.5 – 21.8)

Table 4.5. Properties of continental shelf sediments applicable to this project, including typical ranges from the literature (upper values) and those measured within this project (lower values in brackets).

In sands, the measured and published porosities broadly agree, with the upper limit of the measured porosities greater than those published, while in silts measured values are much greater than those published. Measured densities in sands displayed a wider range than those published, with both ranges centred on similar values of 2013 and 1998 $kg \cdot m^{-3}$ respectively. In silts, measured densities are much less than those published. Caution is raised over the measured density of 881 $kg \cdot m^{-3}$ at Universe 1 (*i.e.* less than that of water) which is attributed to the extremely small sample analysed for this location, *i.e.* a saturated sample which weighed only 20 g. Measured and published proportions of sand are similar in both sands and silts.

The relationships between measured geotechnical properties and those observed in literature, reflect the manner in which these properties were measured within this project (see *Appendix C*). Mean grain size and sand fraction are unaffected by the disturbance of the sample and will be representative of *in situ* values. However, the artificially fast settling time utilised in the laboratory and the destruction of the *in situ* sediment structure will result in measured porosities being greater than those *in situ* and measured densities less than *in situ* values. The effects are more pronounced for silts than sands, owing to the

necessary sieving of the fine-grained portion and the increased dependence of fine-grained sediment structure on inter-particle forces.

As porosity is considered to be the dominant geotechnical property, *Section 2.4.1,* the dependence of bulk density, mean grain diameter and percentage of sand sized particles on porosity were examined, *Figures 4.36* to *4.38.* As no data are available for the intermediate range of very fine sands to coarse silts, empirical fits cannot be applied. The sandy sediments possess lower porosities, higher densities and higher percentages of sand sized particles than for the silty sediments. In sands, density decreases as porosity increases, while no trends are clear in silts. Within the errors and the scatter of the data, no relationship can be observed between either the percentage of sand sized particles and porosity or mean grain diameter and porosity.

Though the few trends which are observed above the scatter and errors agree with those published in the literature, *Section 2.4,* this dataset primarily displays the variability of geotechnical properties in inter-tidal sediments, which arises from the non-uniqueness of the sediment frame, *Section 2.4.1.* Additional factors can also affect sediment structure, namely the sorting and modality of grain size distributions, angularity of the grains and environmental factors such as tidal and wave action.

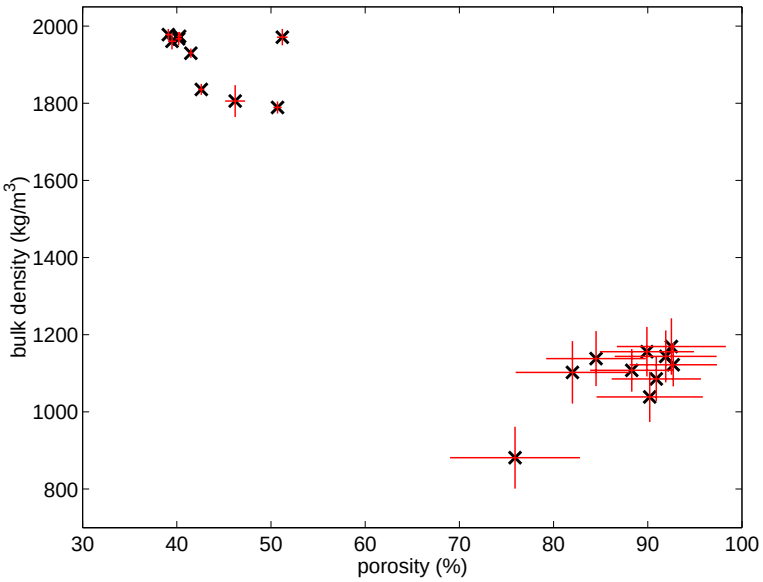

Figure 4.36. Measured bulk density versus measured porosity for the inter-tidal sediment examined, intrinsic errors in both properties, which are calculated as described in Appendix C, are included as red lines.

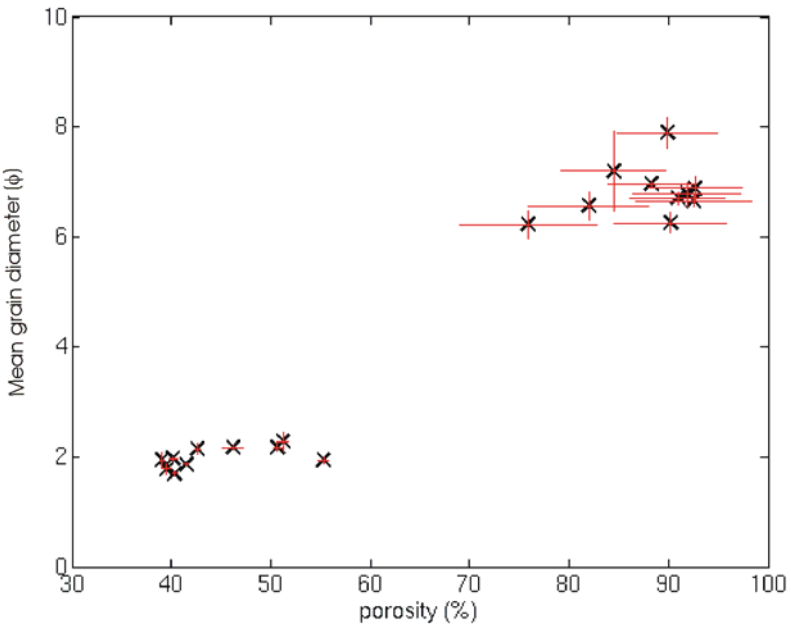

Figure 4.37. Measured mean grain diameter versus measured porosity for inter-tidal sediment examined. Intrinsic errors in porosity, which are calculated as described in Appendix C, and standard deviations in mean grain diameter are included as red lines.

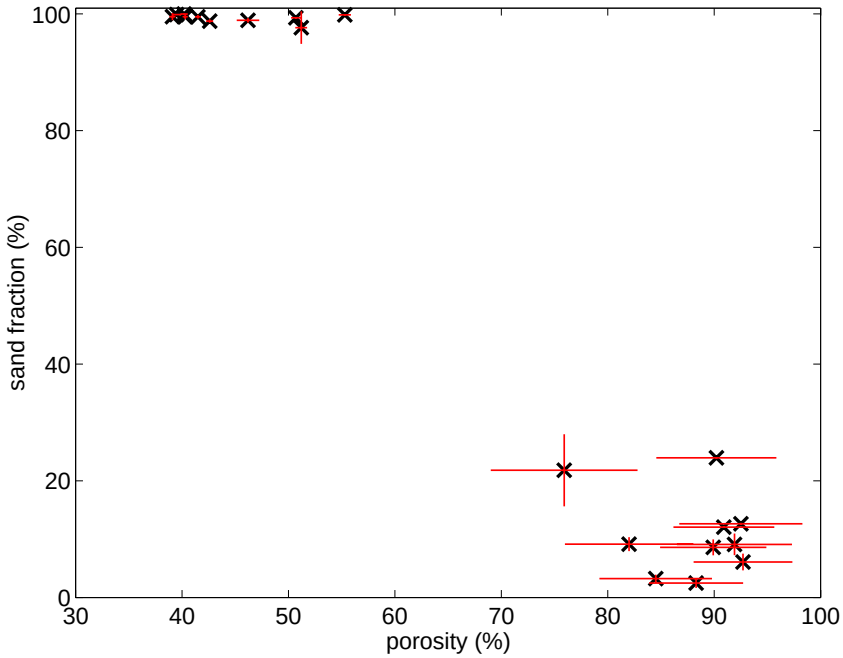

Figure 4.38. Measured percentage of sand sized particles versus measured porosity for inter-tidal sediment examined. Intrinsic errors in porosity, which are calculated as described in Appendix C, and standard deviations in percentage of sand sized particles are included as red lines.

4.5 Summary

A new *in situ* device has been developed, which consists of a source and matched receivers. Both of these probes possess surface areas much greater than *in situ* probes described in the literature, which should permit more repeatable coupling between the probes and the sediment. Combined with the acquisition system developed this can emit and detect pulses with central frequencies between 16 and 100 kHz to a timing accuracy and sampling rate of 1 μs.

Pre-distortion techniques cannot be used to generate an acoustic pulse which possesses a constant amplitude envelope and amplitude without biasing the compressional wave attenuation coefficients measured. Hence care was taken is accurately measure the properties of the electronic pulse across the source transducer. The *in situ* experiments performed within this project use a pre-programmed pulse which possesses a Blackman-Harris spectral envelope and a constant number of oscillations. This generates an amplified pulse across the source transducer with a highly repeatable central frequency, duration, bandwidth and amplitude envelope, and a mean voltage which is repeatable to $\pm$ 5 %. Examination of acoustic waves which have propagated through water conclude that the degree of distortion introduced by the source transducer and receiver is negligible and the amplitude of the received pulses is repeatable to $\pm$ 3.2 %.

A technique has been developed to model the pressure field emitted by the source in any non-dispersive media over a range of compressional wave velocities. The validity of the model was examined through a comparison of pressure fields measured in water and those predicted. Primary acoustic tests confirmed the applicability of the model over the region for which spreading losses are required for the *in situ* transmission experiments. Larger discrepancies between the predicted field and that measured by less well-constrained secondary acoustic tests was attributed to the unknown nature of the electronic pulse applied to the source transducer during these tests.

The model was used to predict the pressure field emitted for the range of compressional wave velocities observed across the inter-tidal sites examined within this project, *i.e.* 1300 to 1800 $m \cdot s^{-1}$. These display a transition from an omnidirectional field at 20 kHz to the dominance of a central lobe for frequencies up to approximately 70 kHz. Between 70 and 90 kHz sidelobes begin to dominate over the central lobe, with no central lobe observable from 90 to 100 kHz. Over the range of frequencies and sediment

examined near to far field transitions lie less than 0.45 m from the source. The assumption that pressure fields are the same in water and sediment would result in errors in amplitude of up to 25 % for sands and 11 % for silts, and is hence inappropriate for typical marine sediments.

A series of *in situ* transmission experiments were performed using the SPADE in a range of inter-tidal sediments. These incorporated deployment methods which induced minimal sediment disturbance. The experimental procedure enabled transmission data to be collected at a range of S-R separations and for pulses with central frequencies from 16 to 100 kHz, in 2 kHz steps. The field-sites selected ensured that the sediment through which the acoustic wave propagated, *i.e.* those lying 1 m below the sediment surface, were saturated. The examination of two to four individual locations at each site allowed the effect of fine-scale variation in geotechnical properties on compressional wave properties to be investigated.

Selected geotechnical properties, *i.e.* porosity, bulk density, mean grain diameter, sorting and percentage of sand sized particles, were measured from sediment samples using standard techniques, while the salinity and temperature of the pore water were also measured. The sediments examined fall into two distinct groups, namely lower porosity sands and higher porosity silts. The variability of the sediment examined at each location was determined, resulting in variations in mean grain diameter less than 12.41 % in sands and 19.83 % in silts. The high degree of scatter in the geotechnical properties measured displays the variability of inter-tidal sediments.